JOURNAL OF GEOPHYSICAL RESEARCH, VOL. 113, C09026, doi:10.1029/2007JC004603, 2008

Oceanic propagation of a potential tsunami from the La Palma Island

F. Løvholt,[1] G. Pedersen,[2] and G. Gisler[3]

Received 22 October 2007; revised 13 June 2008; accepted 25 June 2008; published 16 September 2008.

[1] The likelihood of a large scale tsunami from the La Palma Island is considered small by most. Nevertheless, the potential catastrophic consequences call for attention. Here we report on numerical simulations of a tsunami that might result from the extreme case of a flank collapse of the Cumbre Vieja volcano at the La Palma Island, done by combining a multimaterial model for the wave generation with Boussinesq models for the far-field propagation. Our simulations show that the slide speed is close to critical, effectively generating an initial wave of several hundred meters height. Our main focus is the wave propagation which is genuinely dispersive. In the far-field, propagation becomes increasingly complex due to the combined effects of dispersion, refraction, and interference in the direction of propagation. Constructive interference of the trailing waves are found to decrease the decay of the maximum amplitude with distance compared to classical asymptotic theory at transatlantic distances. Thus, the commonly used hydrostatic models fail to describe the propagation. Consequences of the La Palma scenario would be largest at the Canary Islands, but our findings also suggests that the whole central Atlantic would face grave consequences. However, the largest surface elevations are smaller than the most pessimistic reports found in literature. We also find undular bores towards the shorelines of America.

Citation: Løvholt, F., G. Pedersen, and G. Gisler (2008), Oceanic propagation of a potential tsunami from the La Palma Island *J. Geophys. Res.*, *113*, C09026, doi:10.1029/2007JC004603.

1. Introduction

[2] Within the last decades, submarine landslides have generally been accepted as one of the principal causes of tsunamis in addition to earthquakes. Many historical slide generated tsunamis are now well understood [*Bugge et al.*, 1988; *Bryn et al.*, 2005; *Harbitz*, 1992; *Bondevik et al.*, 2005; *Heezen and Ewing*, 1952; *Fine et al.*, 2005; *Bardet et al.*, 2003]. In particular, the destruction caused by the 1998 Papua New Guinea (PNG) tsunami [*Bardet et al.*, 2003; *Tappin et al.*, 2008] has lead to an increasing awareness of the hazard posed by landslide generated tsunamis. Landslides originating from volcanoes may also generate destructive tsunamis. According to the NOAA/WDC Historical Tsunami Database at NGDC (http://www.ngdc.noaa.gov/seg/hazard/tsu_db.html), the most destructive one was the 1792 Shimabara event causing more than 4000 casualties solely due to the tsunami. In 2002, a landslide originating from the volcanic island of Stromboli, Italy, generated a tsunami that caused local destruction, but no casualties [*Tinti et al.*, 2005]. Herein, we investigate the wave generation and oceanic propagation a potential tsunami due to a flank collapse of the Cumbre Vieja volcano on La Palma in the Canary Islands. We consider solely a single worst case slide scenario and devote the study mainly to the coupling of models and features of transoceanic propagation of the tsunami. Hence, our computed wave heights are not to be read as probable predictions for a future La Palma disaster, but more as a general example of what might be expected from an extreme slide event.

[3] The standard models in long distance tsunami modeling are of the shallow water type. For some tsunamis, in particular those originating from nonseismic sources, such models may not be satisfactory, and dispersive models must be employed instead. Dispersive simulation of the 2004 Indian Ocean tsunami revealed a modest effect of dispersion during deep water propagation [*Ioualalen et al.*, 2007]. However, for the same tsunami dispersive and nonlinear simulations have indicated the undular bores may evolve in shallow water [*Glimsdal et al.*, 2006; *Grue et al.*, 2008]. This phenomenon has been observed for other tsunamis [*Shuto*, 1985] and may be common for earthquake tsunamis. Due to its confined lateral extent end short duration the slump associated with the PNG tsunami probably generated genuinely dispersive waves as demonstrated in the Boussinesq simulations of *Lynett et al.* [2003] and *Tappin et al.* [2008]. Also previous computations of the potential La Palma tsunami have involved dispersive models [*Ward and Day*, 2001; *Mader*, 2001; *Gisler et al.*, 2006; *Perignon*, 2006]. However, none of these works are devoted to investigating the complex wave patterns that may arise when weak dispersion is crucial during long distance propagation. The

[1] Computational Geomechanics Division, Norwegian Geotechnical Institute, Oslo, Norway.
[2] Department of Mathematics, University of Oslo, Oslo, Norway.
[3] Physics Department, University of Oslo, Oslo, Norway.

0148-0227/08/2007JC004603$09.00

particular scenario for the La Palma tsunami studied herein is an excellent example on this kind of behavior.

[4] At least 14 large submarine landslides from the flanks off La Palma, Tenerife and El-Hierro are evident from seabed surveys near the Canary Islands [*Masson et al.*, 2002, 2006; *Krastel et al.*, 2001]. The last event occurred about 15 000 years ago on the Island of El-Hierro. Most of the Canary Island landslides have occurred within the last 1 million years [*Masson et al.*, 2002], giving an average occurrence cycle of approximately 100 000 years. Typical volumes of the slide deposits range from 50–200 km^3 [*Masson et al.*, 2006]. However, core samples of turbidite deposits from the Agadir basin north of the Canary Islands [*Wynn and Masson*, 2003], suggest that the landslides have developed through multistage processes, probably with separation times ranging from hours to days. Such a process with large separation times is obviously less efficient in generating the tsunami than if the whole volume is released simultaneously. Large-scale landslides from volcanic islands are also found off the Hawaii islands [*Moore et al.*, 1989], the largest one being the Nuuanu landslide with a volume of 5000 km^3. In fact, the Hawaiian landslides tend to be a magnitude larger than the Canary Islands landslides [*Masson et al.*, 2006]. There is evidence that indicates that the Hawaiian landslides also have developed in a retrogressive fashion, as their turbidite deposits [*Garcia*, 1996] follows the characteristics observed for the Canary Islands [*Wynn and Masson*, 2003]. In addition, there exists a number of large-scale landslides originating from the West African margin, examples are found in *Masson et al.* [2006].

[5] As a consequence of the expected multistage development, an event with simultaneous release of volumes up to 500 km^3 as suggested by *Ward and Day* [2001] is by many considered unlikely [*Masson et al.*, 2006; *Wynn and Masson*, 2003; *Pararas-Carayannis*, 2002]. Thus the occurrence rate of such an event should at least be clearly lower than the frequency of slide events in the Canaries. On the other hand, the extreme scenario cannot be completely ruled out. It is also noted that extreme tsunami scenarios with low probabilities may give large consequences, which could lead to a larger risk compared to a smaller and more probable scenario [*Nadim and Glade*, 2006]. In the following, we do not address the likelihood of the investigated extreme case scenario further, but study its consequences.

[6] Of all the volcanoes on the Canary Islands, the Cumbre Vieja volcano on La Palma Island is the one growing most rapidly [*Carracedo et al.*, 1999]. Hence, it poses a threat with respect to potential landslides and tsunamis. *Ward and Day* [2001] modeled a potential tsunami generated by a flank collapse of the Cumbre Vieja volcano with a linear fully dispersive ray model, for a slide volume of 500 km^3. Enormous waves were reported, for example surface elevations up to 20–25 m for the coastlines of Florida. However, other modeling attempts using similar slide volumes report much smaller waves [*Gisler et al.*, 2006; *Mader*, 2001]. *Mader* [2001] applied a nonlinear shallow water model (NLSW) to simulate the wave propagation in two-horizontal dimensions. To account for frequency dispersion, he used a Navier-Stokes model for plane waves with a simplified monopole source as initial condition. Combining the results of the two models and assuming uniform radial spread, he found an order of magnitude smaller waves in the far field compared to *Ward and Day* [2001].

[7] Applying the multimaterial model SAGE, *Gisler et al.* [2006] simulated the combined propagation of the landslide and the near field tsunami. The present work is a continuation of *Gisler et al.* [2006] (their work is briefly reviewed in section 3) and addresses something near to a worst case scenario concerning slide volume and speed, even though smaller events may be more probable (see discussion above). Our focus is on the modeling and description of the oceanic evolution of waves from such a giant slide. Different models are applied to the wave generation and propagation, as described in section 2. For the wave propagation, we use depth averaged quantities from SAGE as initial conditions for tsunami simulations in cylindrical symmetry and two horizontal dimensions (2HD), applying a finite difference Boussinesq model including the Coriolis terms. Model comparisons and investigations of asymptotic behavior in simplified geometries applying cylindrically symmetric models are described in section 4. Simulations of the wave propagation in real geometries and a brief discussion of possible consequences are given in sections 5–6, for the Canary Islands and the central Atlantic Ocean respectively. Owing to the complexity of the present case, the focus of this paper is to explain wave propagation effects. Therefore, runup simulations are not included, except at La Palma Island.

[8] As the preceding studies [*Ward and Day*, 2001; *Mader*, 2001], this work focuses on an extreme case scenario. However, the present work, together with *Gisler et al.* [2006], differs from the other attempts to model the La Palma tsunami, as they include dissipative effects of wave-breaking and turbulence during generation, as well as dispersive propagation simulations without constraints on the wave directivity. In fact, combinations of multimaterial models including deformable slides with transoceanic wave computations of this scale, are not found in any papers for this particular application to this day. Likewise, a detailed investigation on the evolution of the crests in the dispersive wave train is not found in any papers the authors are aware of.

2. Modeling Strategy

[9] The wave generation is simulated by the multimaterial code SAGE, whereas depth averaged Boussinesq type models are used for the wave propagation modeling. Simulations in both one horizontal dimension utilizing cylindrical symmetry and in 2HD are conducted.

[10] For the far field tsunami propagation we employ geographical co-ordinates with horizontal axes $o\psi$ and $o\varphi$, in the longitudinal and latitudinal directions respectively. In the near field computations, on the other hand, Cartesian systems are used. While graphs and tables are given with dimensions, long wave equations are written in their more common nondimensional form. We denote the surface elevation as η, the equilibrium water depth as h, and the horizontal velocities components as u and v. Normally, u and v are positive in the eastward and northward directions, respectively.

2.1. Examples of Previous Wave Generation and Slide Models

[11] Submarine landslides evolve in different ways, as nondeformable slides and slumps, dense or suspended flows, but often as combinations of such [*Hampton et al.*,

1996]. The simplest models for modeling landslides are block models [*Perla et al.*, 1980], which may be successfully applied to slides with no or little internal deformation. Debris flows may extend over large geographical areas, their evolution is often simulated using depth averaged models [*Locat and Lee*, 2002; *Elverhøi et al.*, 2005]. For the tsunamigenic dense part of flowing slides, simple Bingham fluids, generalized Herschel-Buckley rheologies, or bi-linear models have traditionally been used, parameterizing the yield strength as a power law function of the strain rate in the sliding material [*Imran et al.*, 2001]. In addition, models combining the description of the full flow field with more advanced rheologies have more recently been successfully applied, one example is a model of the the last phase of the 8150 BP Storegga slide using a strain softening material model [*Gauer et al.*, 2005].

[12] Wave generation by landslides has been studied previously both experimentally [*Fritz et al.*, 2003a, 2003b; *Walder et al.*, 2003], by full hydrodynamic models [*Mader*, 2004; *Abadie et al.*, 2006; *Jiang and LeBlond*, 1992], and by combining the two [*Liu et al.*, 2005]. Using a nonlinear full potential model, *Grilli and Watts* [2005] reproduced laboratory experiments of waves generated by a rigid body, fully submerged landslide. *Fritz et al.* [2004] found that the initial crest amplitude generally depends strongly upon the Froude number (ratio of slide speed to wave celerity), as well as the frontal slide area. The wave generation is defined as critical when the Froude number is close to unity, and the slide is then efficient in generating waves. Here, we apply the multimaterial model SAGE for the wave generation, whereas dispersive long wave models are used for the modeling of the far-field tsunami propagation. Fully compressible flow models have been successful in modeling the 1952 Lituya Bay tsunami [*Miller*, 1960; *Mader*, 1999; *Mader and Gittings*, 2002], showing good agreement with both experimental data [*Fritz et al.*, 2004] as well as observed runup.

2.2. SAGE Model

[13] The SAGE hydrocode is a multimaterial adaptive-grid Eulerian code with a high-resolution Godunov scheme originally developed by *Gittings et al.* [2006] for Science Applications International (SAIC) and Los Alamos National Laboratory (LANL). The grid refinement is dynamic, cell by cell and cycle by cycle throughout a simulation. Refinement occurs when gradients in physical properties (density, pressure, temperature, material constitution) exceed user-defined limits, down to minimum cell sizes specified by the user. With the computing power concentrated on the regions of the problem that require higher resolution, very large computational volumes and substantial differences in scale can be simulated at an affordable cost. Details regarding the numerical techniques employed in SAGE is elaborated in Appendix A.

[14] The SAGE code solves the generalized Euler equations

$$\frac{\partial \rho}{\partial t} = -\nabla \cdot (\rho \vec{u}) \tag{1}$$

$$\frac{\partial \rho \vec{u}}{\partial t} = -\nabla \cdot (\rho \vec{u}\vec{u}) - \nabla \cdot \overleftrightarrow{\sigma} \tag{2}$$

$$\frac{\partial \rho E}{\partial t} = -\nabla \cdot (\rho \vec{u} E) - \nabla \cdot \left(\overleftrightarrow{\sigma} \cdot \vec{u} \right) \tag{3}$$

where ρ is density, $\vec{u}$ is velocity, E is specific internal energy, and $\overleftrightarrow{\sigma}$ is the full stress tensor. Gravitational terms are added to the momentum and energy equations, and then the set above is supplemented by a constitutive relation

$$\overleftrightarrow{\sigma} = \overleftrightarrow{F}(\rho, E, t, ...) \tag{4}$$

prescribed for every material in the problem. The constitutive relation includes both equations of state and strength models. Both are available in a variety of analytic and tabular forms. For the landslide-induced tsunami model described here we use a special tabular equation of state for water from SAIC, and LANL SESAME tabular equations of state for the completely fluidized rock and air. The basement of La Palma and the seafloor are treated as unmoving reflective boundaries, while the other boundaries are designed to allow unrestricted outflow.

2.3. Boussinesq Models

[15] As demonstrated subsequently we need a Boussinesq type model for global wave propagation. The standard models freely available from the Internet, such as the FUNWAVE [*Kirby et al.*, 1998; *Kirby*, 1998] and COULWAVE [*Lynett and Liu*, 2004] models, are originally designed for other purposes with emphasis on full nonlinearity. In addition the available versions of these models do not include geographical co-ordinates or the Coriolis effect, even though the implementation of such effects in FUNWAVE has been briefly reported [*Kirby et al.*, 2004]. Hence, we have developed a new Boussinesq solver particularly suited for global applications. Details are given in *Pedersen and Løvholt* [2008] and we only refer a few key points herein.

[16] To write the equations in standard form we introduce dimensionless variables according to

$$(\psi, \phi) = \Theta(\hat{x}, \hat{y}), \qquad \hat{t} = \frac{R\Theta}{\sqrt{g h_0}}$$

$$(u, v) = \epsilon \sqrt{g h_0}(\hat{u}, \hat{v}) \quad h = h_0 \hat{h} \quad \eta = \epsilon h_0 \hat{\eta} \tag{5}$$

where the hats indicate dimensionless variables, g is the constant of gravity, h_0 is a characteristic depth and ϵ is an amplitude factor. The characteristic horizontal length (wave length) now becomes $L_c = R\Theta$, which may determine Θ, and the "long wave parameter" is accordingly recognized as $\mu^2 = h_0^2/(R^2\Theta^2)$. For the physical constants we substitute for $g = 9.81$ m/s^2 and for the Earth's equatorial radius $R = 6378135$ m. It is recognized that these quantities are not constant, but their variation is neglected along with other small effects of the rotation and curvature of the Earth.

[17] Rotational effects are included simply by adding the Coriolis term to the momentum equation. According to the length and time scale inherent in (5) we obtain a nondimensional Coriolis parameter $f = 2\Omega R\Theta \sin\phi/\sqrt{g h_0}$, where Ω is the angular frequency of the Earth.

[18] By omission of the hats the dimensionless equation of continuity in geographical coordinates reads

$$c_\phi \frac{\partial \eta}{\partial t} = -\frac{\partial}{\partial x}[(h + \epsilon\eta)u] - \frac{\partial}{\partial y}\left[c_\phi (h + \epsilon\eta)v\right], \tag{6}$$

where $c_\phi = \cos\phi$ and u, v are interpreted as vertically averaged velocity components. The momentum equations read

$$\frac{\partial u}{\partial t} + \epsilon\left(\frac{u}{c_\phi}\frac{\partial u}{\partial x} + v\frac{\partial u}{\partial y}\right) = -\frac{1}{c_\phi}\frac{\partial \eta}{\partial x} + fv - \gamma\mu^2 h^2 \frac{1}{c_\phi}\frac{\partial D_\eta}{\partial x} + \frac{\mu^2}{2}\frac{h}{c_\phi^2}\frac{\partial}{\partial x} \cdot \left[\frac{\partial}{\partial x}\left(h\frac{\partial u}{\partial t}\right) + \frac{\partial}{\partial y}\left(c_\phi h\frac{\partial v}{\partial t}\right)\right] - \mu^2\left(\frac{1}{6}+\gamma\right)\frac{h^2}{c_\phi^2}\frac{\partial}{\partial x} \cdot \left[\frac{\partial}{\partial x}\left(\frac{\partial u}{\partial t}\right) + \frac{\partial}{\partial y}\left(c_\phi\frac{\partial v}{\partial t}\right)\right],$$

$$\frac{\partial v}{\partial t} + \epsilon\left(\frac{u}{c_\phi}\frac{\partial v}{\partial x} + v\frac{\partial v}{\partial y}\right) = -\frac{\partial \eta}{\partial y} - fu - \gamma\mu^2 h^2\frac{\partial D_\eta}{\partial y} + \frac{\mu^2}{2}h\frac{\partial}{\partial y} \cdot \left[\frac{1}{c_\phi}\frac{\partial}{\partial x}\left(h\frac{\partial u}{\partial t}\right) + \frac{1}{c_\phi}\frac{\partial}{\partial y}\left(c_\phi h\frac{\partial v}{\partial t}\right)\right] - \mu^2\left(\frac{1}{6}+\gamma\right)h^2\frac{\partial}{\partial y} \cdot \left[\frac{1}{c_\phi}\frac{\partial}{\partial x}\left(\frac{\partial u}{\partial t}\right) + \frac{1}{c_\phi}\frac{\partial}{\partial y}\left(c_\phi\frac{\partial v}{\partial t}\right)\right], \quad (7)$$

where $D\eta$ is the dimensionless Laplacian of η

$$D\eta = \frac{1}{c_\phi}\left[\frac{\partial}{\partial x}\left(\frac{1}{c_\phi}\frac{\partial \eta}{\partial x}\right) + \frac{\partial}{\partial y}\left(c_\phi\frac{\partial \eta}{\partial y}\right)\right].$$

Putting γ equal to zero we retrieve the standard Boussinesq equations [*Peregrine*, 1967], while the $\gamma = -0.057$ yields the same improved dispersion properties as in the formulation of *Nwogu* [1993]. The numerical solution procedure for (6) and (7) is described briefly in Appendix B. A full treatise of the method is found in the companion technical report [*Pedersen and Løvholt*, 2008].

[19] In the radially symmetric description we ignore the Coriolis effect and the curvature of the Earth to obtain

$$\frac{\partial \eta}{\partial t} = -\frac{1}{r}\frac{\partial}{\partial r}\left(r\left\{(h+\epsilon\eta) + \mu^2 M\right\}\right) \quad (8)$$

$$\frac{\partial u}{\partial t} + \epsilon u\frac{\partial u}{\partial r} = \quad (9)$$

$$-\frac{\partial \eta}{\partial r} + \mu^2 F\frac{\partial}{\partial r}\left[\frac{1}{r}\frac{\partial}{\partial r}\left(rh\frac{\partial u}{\partial t}\right)\right] + \mu^2 G\frac{\partial}{\partial r}\left[\frac{1}{r}\frac{\partial}{\partial r}\left(r\frac{\partial u}{\partial t}\right)\right], \quad (10)$$

where r is the distance from the center of symmetry. The above set contains two different formulations. If we substitute $M = 0$, $F = \frac{1}{2}h$ and $G = \frac{1}{6}h^2$ we obtain the cylindrical counterpart of the standard equations. On the other hand, $F = z_\alpha$, $G = \frac{1}{2}z_\alpha^2$ and

$$M = \left(\frac{1}{2}z_\alpha^2 - \frac{1}{6}h^2\right)\frac{\partial}{\partial r}\left[\frac{1}{r}\frac{\partial}{\partial r}(ru)\right] + \left(z_\alpha + \frac{1}{2}h\right)\frac{\partial}{\partial r}\left[\frac{1}{r}\frac{\partial}{\partial r}(rhu)\right],$$

reproduce the formulation of *Nwogu* [1993]. In this case the u is the velocity at vertical position z_α. The favorable z_α, that is used also herein, is $-0.531h$. We solve both versions of (8) with a procedure similar to that used for (6) and (7). However, for the radial versions the implicit equations are tri-diagonal and no iteration is required.

2.4. Asymptotic Behavior of Long Waves

[20] For the subsequent discussion, asymptotic expressions for the wavefront of linear dispersive long waves at large times are useful. For plane waves, we follow the textbook of *Mei* [1989] pp. 30–35, and write

$$\eta \propto \frac{V}{2}\left(\frac{2}{c_0 h^2 t}\right)^{1/3}\mathrm{Ai}\left(\left(\frac{2}{c_0 h^2 t}\right)^{1/3}[x - c_0 t]\right), \quad (11)$$

for a monopole like source with a net integrated displacement V. If the net integrated displacement is zero, and the initial surface elevation is anti-symmetric, we may write

$$\eta \propto \frac{B}{2}\left(\frac{2}{c_0 h^2 t}\right)^{2/3}\mathrm{Ai}'\left(\left(\frac{2}{c_0 h^2 t}\right)^{1/3}[x - c_0 t]\right), \quad (12)$$

for a dipole like source. Ai and Ai′ defines Airy's function and its derivative respectively, and c_0 is the linear hydrostatic wave celerity. The dipole moment B is found by integrating the anti-symmetric initial surface elevation $\eta_0(x)$ according to

$$B = \int_{-\infty}^{\infty} x\eta_0(x)dx. \quad (13)$$

The front of the monopole-like source decays by a rate of $t^{-1/3}$, the front of the dipole like source decays by $t^{-2/3}$, and the trailing waves by $t^{-1/2}$. Near the front, we have $x/t \approx c_0$, which gives approximate expressions $x^{-1/3}$, $x^{-2/3}$, and $x^{-1/2}$ respectively, as functions of the distance. Substituting $x \to r$ in a radial symmetry of radius r assuming a uniform geometric spread of $r^{-1/2}$ give the corresponding figures $r^{-5/6}$, $r^{-7/6}$, and r^{-1} respectively. For the net positive surface elevation imposed by a sub-aerial landslide, we therefore expect a $r^{-5/6}$ decay for the leading wave after large propagation times. In general, we may write the asymptotic decay as

$$\eta = \eta_0 r^{-\alpha}, \quad (14)$$

where η_0 is a constant. By differentiating equation (14) once, we define an instantaneous value

$$\alpha = \frac{\eta'}{\eta}r. \quad (15)$$

We also note that the asymptotic wavelength scales as $\lambda \propto x^{1/3}$.

2.5. Methods for Quantifying Data Set Deviations

[21] Throughout the paper, deviations between data sets arising from different numerical simulations are quantified with respect to some reference solution. The deviations are encountered in grid refinement tests or when different models are compared, using snapshots of the surface elevation along transects, e.g. by comparing the maximum surface elevation for a given crest $\eta_{\max}$ to a reference solution $\eta_{\max,ref}$ using the relative amplitude deviation L_{ampl} defined by

$$L_{ampl} = \frac{\left|\eta_{\max} - \eta_{\max,ref}\right|}{\left|\eta_{\max,ref}\right|}. \quad (16)$$

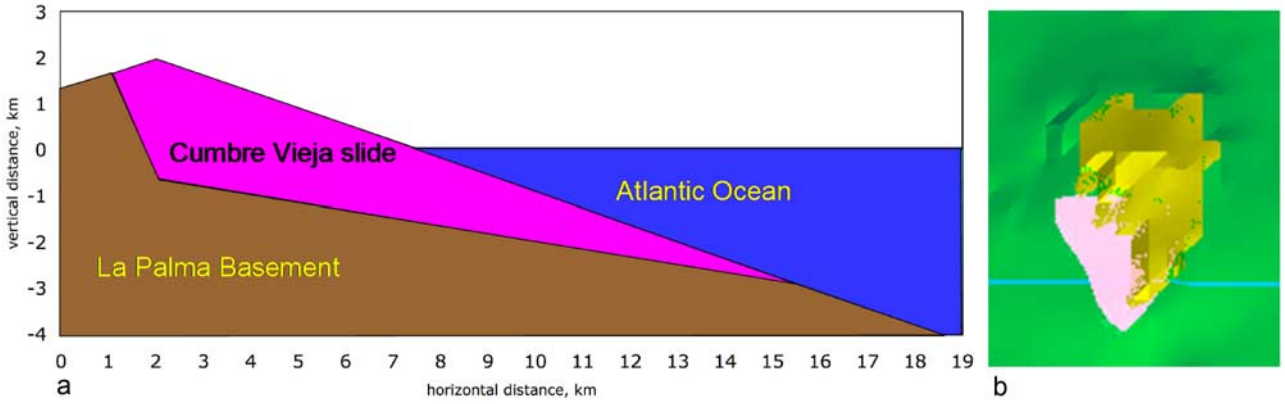

Figure 1. (a) Transect showing a principle sketch of the slide configuration used for the cylindrically symmetric simulations. (b) Sketch region around La Palma indicating the ocean bottom (in green), the above-water portions of the islands (in yellow), and the slide region (in pink).

Alternatively, we may quantify the relative $L_2(\eta_1, \eta_2, x_1, x_2)$ norm defined over an interval $x_1 - x_2$ for a variable grid resolution Δx_i by

$$L_2(\eta_1, \eta_2, x_1, x_2) = \sqrt{\frac{\Sigma\left[(\eta_1 - \eta_2)^2 \Delta x_i^2\right]}{\Sigma\left(\eta_2^2 \Delta x_i^2\right)}}. \tag{17}$$

Generally, η_1 is interpolated linearly on η_2 before subtraction. In this paper, both methods are used as alternative deviation measures for the same data set, quantifying the deviations in η for a finite segment of the wave including a single crest and through.

2.6. Conversion of Full Flow Fields to the Boussinesq Models

[22] From the mixed cells in SAGE material interfaces are inferred and extracted to the Boussinesq models as surface elevation and water depth. The horizontal velocity components are found by averaging through the vertical water column, and used as initial conditions. For the special case of the cylindrical symmetric optimized velocity model, we first find the expression for the mean velocity $\bar{u}$ by depth averaging the velocity profile given by equation (23) in *Nwogu* [1993], and then we discretize the second order differential equation that arises for the velocity u_α at a depth z_α given by

$$\bar{u} = u_\alpha + \mu^2 \left(\left(\frac{z_\alpha^2}{2} - \frac{h^2}{6} \right) \frac{d}{dr} \left(\frac{1}{r} \frac{d(ru_\alpha)}{dr} \right) + \left(z_\alpha + \frac{h}{2} \right) \frac{d}{dr} \left(\frac{1}{r} \frac{d(rhu_\alpha)}{dr} \right) \right) + O(\mu^4), \tag{18}$$

using centered differences. A difference from the original formulation of *Nwogu* [1993], is the radial differential operator in equation (18).

3. Wave Generation

[23] The SAGE code is applied to a series of cylindrical symmetric and three-dimensional (3-D) configurations designed to resemble the potential flank collapse on Cumbre Vieja. Details of these calculations are found in *Gisler et al.* [2006]. At the beginning of the calculation the slide material sits above the reflecting basement, filling in the quadrilateral formed by a straight line connecting the knee (at about 13 km) to the island summit, then down to the tip of the reflecting region on the y axis. This geometry is a simplified schematic suggested by S. Day (personal communication, 2006) for our cylindrical symmetric calculations (see Figure 1).

[24] The slide material is a fluid with the density of basalt (representing granules), and it begins to flow under the influence of gravity as soon as the calculation begins. The material flow first pushes the water above the lower part of the slide up, and then, later, craters the water at the rear of the slide. As the slide progresses, hydrodynamic instabilities between the water and slide material produce turbidity currents and swirls in the water/granular rock mixture. These will eventually be left as turbidite deposits, similar to what is already seen around several of the Canary Islands from old slide events. The progression of the slide along the bottom continues to pump energy into the water wave that is driven ahead of it, until the hydrodynamic drag and friction with the bottom (not included in the calculations) slow and eventually stop the slide run-out.

[25] The maximum speed of the slide is 190 m/s giving a Froude number of 0.96, and is thus effective in generating a high leading wave localized just ahead of the slide front as shown in Figure 2. The turbulent flow visible behind the front of the slide generates shorter but smaller wave components of lesser importance for the distant propagation. As the slide decelerates throughout the later stage of motion, the leading wave separates from the slide front, while trailing waves of shorter wave components continue to appear, giving altogether a complex initial wave shape of many crests and troughs. A snapshot from a plane 2-D calculation by *Gisler et al.* [2006] is shown in Figure 2 at 200 s after the start of the landslide. *Gisler et al.* [2006] studied the effects of slide rheology for the La Palma scenario on the characteristics of the water wave, finding that for a given time, the slide speed is reduced by from 148 m/s to 132 m/s for the case of a viscid slide. The inviscid slide used for the calculations here therefore represents the worst case also with respect to the slide speed. Convergence of the SAGE solution for landslide-induced tsunamis similar to the La Palma scenario have previously been studied by *Gisler* [2008]. He found that the

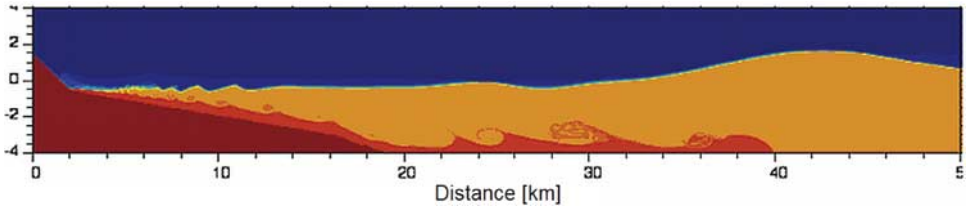

Figure 2. Snapshot of a two-dimensional SAGE simulation 200 s after slide release. This graphic is a density raster plot, with air showing up blue, water orange, and the slide material red. In brown at bottom left is the unmoving basement, an internal reflecting boundary that otherwise does not participate in the calculation. Only a small portion of the computational volume is shown; the downstream boundary is located at 120 km.

finer grid gave more detailed dynamics on the slide/water interface, displaying a series of vortexes linked to shear instabilities, but that the generated water wave was less sensitive to the grid resolution.

[26] In our 3-D calculations, we used ETOPO 2 data of bathymetric and topographic data for the region around La Palma, refined to a resolution of 125 m used for the computations. Unfortunately this data is coarsely resolved, but for the purpose of examining a synthetic scenario, it was considered applicable. We set up the slide by making a cut formed by the intersection of two vertical cylinders to approximate the slide region considered by *Ward and Day* [2001]. We varied the parameters of the cut in order to maximize the slide volume in accordance with S. Day (personal communication, 2006), but could not produce a volume greater than 375 km^3 by this means. This volume was used in our 3-D computations, and it is illustrated in Figure 1. Onshore, the volume covers an area of the south- western tip of the island affecting some 21 km to the north and almost the entire width. Offshore, the affected area extends some 5–10 km southwesterly into the ocean. Because of the expense and time associated with doing 3-D full hydrodynamic simulations, we have not investigated the sensitivity of the resulting wave to the geometry or size of this source, and felt in any case that doing so was not justified by the low quality of the bathymetry as well as the uncertainty of the scenario. It was, and still is, our intention to perform higher resolution studies on a more probable slide scenario when we gain access to appropriate bathymetric data. The slide in 3-D behaves very similarly to the cylindrically symmetric calculation, but the water wave now has the opportunity to spread azimuthally, diminishing the wave height somewhat.

[27] In the following, we will apply the cylindrical symmetric and 3-D results as input to Boussinesq simulations for the continued propagation. The slide applied for the cylindrically symmetric simulations also corresponds to the scenario labeled Cth31 in *Gisler et al.* [2006], with a volume of 473 km^3.

4. Wave Simulations in Cylindrical Symmetry

[28] The surface elevation, velocity, and depth from the cylindrical symmetric SAGE simulations at 300 s are used as initial conditions to the standard Boussinesq model and the optimized Boussinesq model based on Nwogu's equations, for a grid resolution of $\Delta r = 0.78$ km. Figure 3 shows the surface elevation in SAGE after 300 s, and a comparison of the surface elevations from both the SAGE simulation and the Boussinesq models after 450 s. The dominating leading wave in the SAGE simulation is satisfactorily reproduced in both the Boussinesq simulations. Moreover, the leading waves of the two different Boussinesq models are more or less indistinguishable, with an amplitude deviation of 1%. The Boussinesq models reproduce the wavelengths of the trailing waves, but the amplitudes are exceeding the ones in the SAGE model (in particular the standard model, less so the optimized). Because the Boussinesq simulations do not include wave generation effects, the agreement for the trailing wave system for the optimized model indicates that the dominant part of the wave generation has taken place within 300 s.

[29] It is noted that the slide is still in motion when the SAGE simulation is terminated at 450 s, and that vorticity is present in the water column following the leading wave. The waves evolving from the initial trailing waves are therefore described less accurately by the Boussinesq models. Because they are also smaller than the leading wave, we focus on the waves evolving from the leading wave-system in the following. The error of employing a Boussinesq model, using the SAGE results at 450 s as initial condition, will be even smaller than shown in Figure 3, because the relative importance of effects such as turbulence and wave breaking are expected to decrease as the wave moves away from the generation area.

4.1. Model Comparisons

[30] Simulations with different depth averaged models are performed for quantifying model differences. The SAGE result at 450 s is used as initial condition, on a profile with an elongated constant depth of $h = 4$ km, allowing the waves to propagate over distances of more than 20000 km.

[31] The first comparison includes a selection of models, including LSW, NLSW, optimized and standard Boussinesq models; for the latter also the linear version. Figure 4 shows that after 20 min 58 s of propagation, the standard and optimized Boussinesq models are in close agreement, whereas wave shapes of the linear dispersive and hydrostatic models (NLSW and LSW) all deviate. For the NLSW model, the solution will eventually break, evident from the secondary crest at $r \approx 210$ km. However, the Boussinesq models show that such steep waves will not develop at this stage. Using the optimized Boussinesq model as a reference, we find amplitude deviations of 0.9%, 12.2%, 58%, and 61% for the standard Boussinesq, linear dispersive, LSW, and NLSW models respectively. Hence, dispersive models are needed to describe the wave evolution, and nonlinear

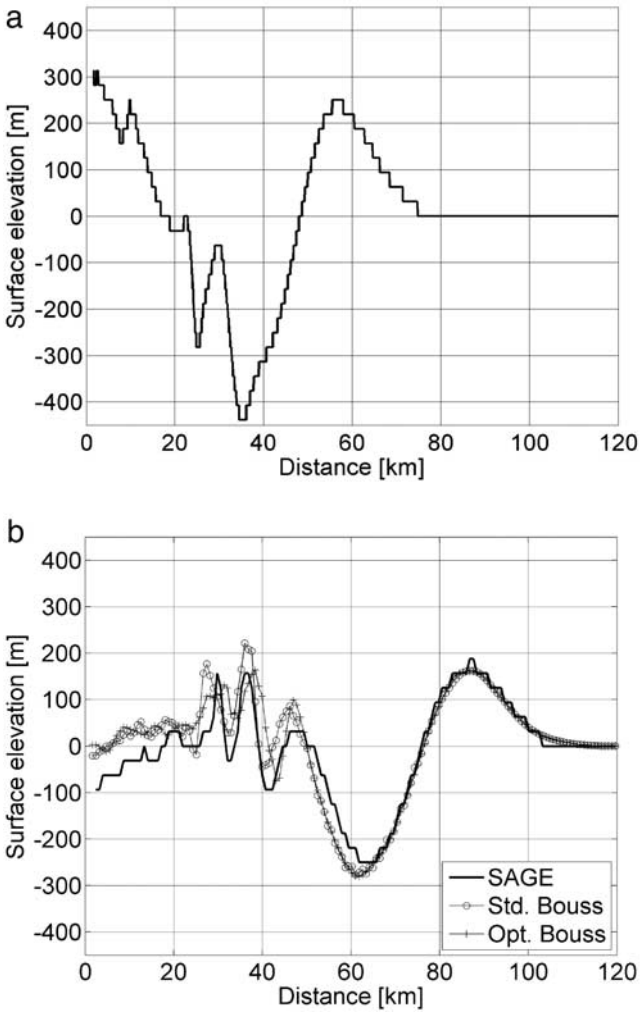

Figure 3. (a) Surface elevation from SAGE at t = 300 s. (b) Surface elevation from SAGE, standard Boussinesq model, and optimized Boussinesq model at t = 450 s.

effects are only moderate for the first 300 km of wave propagation. Finally, we note that for a propagation time of 5 hours, comparison of the standard and optimized Boussinesq models only gives amplitude deviations of order 0.1%, 1% and 1–2% for the first, second, and third crest respectively. Hence, higher order dispersion during propagation is probably not important for this event.

4.2. Evolution of the Wavefield

[32] First we perform grid refinement tests with resolutions $\Delta r = 0.78$ km and $\Delta r = 0.37$ km using $\Delta r = 0.183$ km as a reference grid and Courant numbers in the range 0.1–1. We find amplitude deviations of 1–0.1% for the first three wave crests.

[33] For the subsequent cylindrical simulations we continue with the 0.78 km grid resolution, and simplify the initial conditions by removing all wave components of the tail given in Figure 3 (i.e., by setting $\eta = u = 0$ for $r < 50$ km). This simplifications are performed because we are interested in the interaction of the leading crest and trough, in addition the initial trailing waves are of secondary importance for the evolution of the leading wave system. Since a part of the slide starts subaerially the net surface elevation of this scenario is positive, with the ratio of the integrated elevation to the integrated depression close to unity (1.03). Figure 5 shows the simulated surface elevations compared with asymptotic expressions for the crest heights in the far field.

[34] By inspecting Figure 4 we see that in the first 300 km of propagation, the dispersive wave train starts to develop, whereas Figure 5 shows that the wave-system in the far field is dominated by the trailing wave system. The decay α is computed numerically at intermediate positions between the computed crest elevations, by using centered differences for η' and taking the means for η and r. In Figure 6, α is shown as a function of r for the leading, second, and third crest. The leading crest decays faster than r^{-1} both in the near field and the far field. As there is a net positive surface elevation, the leading crest is expected to eventually decay as $r^{-5/6}$ as noted in section 2.4. However, the net surface elevation is much smaller than the individual elevation and

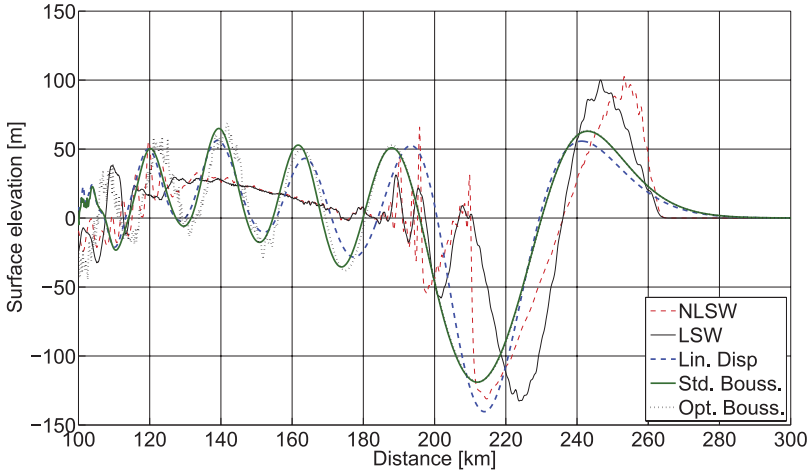

Figure 4. Surface elevation in the radial geometry 20 min 58 s after the slide release using standard and optimized Boussinesq, linear dispersive, NLSW, and LSW models.

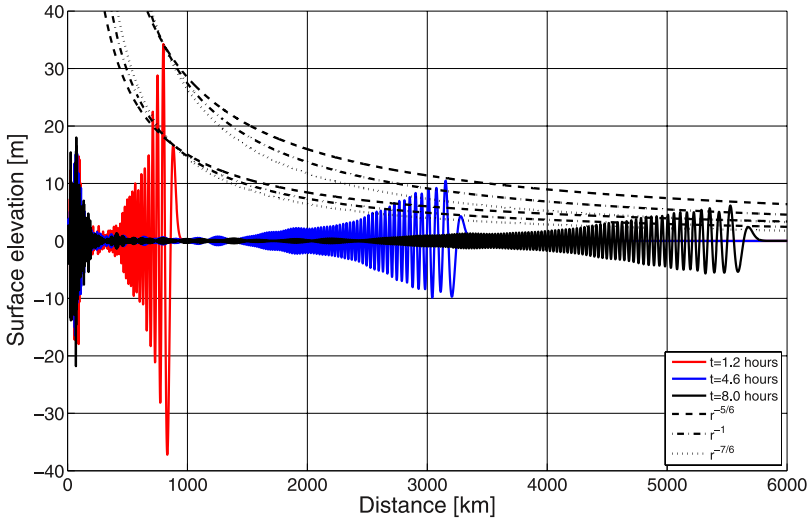

Figure 5. Evolution of the wavefield in radial geometry using a simplified source. Distances up to 6000 km.

troughs. The observed decay rate might therefore exhibit behavior intermediate between a monopole-like and a dipole-like. Figure 6 shows that the trailing wave decay vary as a function of distance, and tends to be slower than the asymptotic value of r^{-1} along most of the propagation path. Hence, the largest crests of the wave train decay slower than expected from asymptotic theory for a long distance of propagation, presumably owing to the effect of constructive interference between the leading elevation and the, only slightly smaller, trailing trough generated by the slide. This effect must not be confused with the interference due to bathymetric features in the oceanic propagation. It is noted that a distance of 5000 km corresponds to the distance across the Atlantic, whereas 20000 km is approximately half the circumference of the Earth. As illustrated, there may therefore be different asymptotic regimes, and the transition times between them may be large. In addition to the simulations described above, a series of simulations using synthetic initial conditions similar to the one above have shown that the asymptotic solutions are sensitive to the distribution of the ratio initial crest and through elevations as well as their separation distance (results not shown).

[35] Finally, it is noted that a previous simulation with a Navier-Stokes model of the La Palma scenario for plane waves in constant depth [*Mader*, 2001], found a monopole-like behavior, using a simple source with no initial depression. The more complex evolution of the wave-system shown in Figure 5, comes as result of the dipole-like shape of the source, and differs clearly from the findings of *Mader* [2001]. For such sources excluding the initial depression, important mechanisms in the subsequent wave propagation are lost.

[36] In the following, we will not pursue the radial simulations further. Instead, we turn the attention to the 2HD simulations.

5. Tsunami Propagation Close to the Canary Islands

[37] For propagation in the Canary Islands region, we apply the standard 2HD Boussinesq model, using the surface elevation shown in Figure 7 and the velocity extracted from the three-dimensional SAGE simulations at 300 s as initial conditions. Artificial boundary reflections in SAGE north of y = 3190 km and south of y = 3130 km are removed. The SAGE fields used in the Boussinesq simulations are given as west-east slices with grid resolutions Δx = 0.625 km, with a north-south spacing of Δy = 2.0 km. A small portion of the slide masses were moving eastward, as a result generating waves at the east side of La Palma. These waves were neglected in the propagation analysis.

5.1. Computational Grid

[38] The bathymetry is modified from ETOPO 2, and shown in Figure 8. For the first 300–600 s of propagation we apply a Cartesian grid with resolution $\Delta x = \Delta y$ = 0.75 km, and with smoothed coastlines. For the subsequent simulations the fields from the Cartesian system were projected to the geographical co-ordinates using a fixed spacing in longitude-latitude giving a projection error of less than 1%. To avoid instabilities from nonlinear terms in the absence of an inundation model, we limit

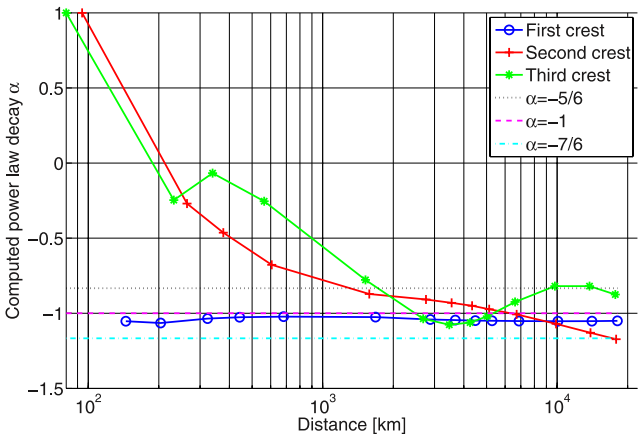

Figure 6. Power law decay for the leading, second and third crests, compared with asymptotic solutions.

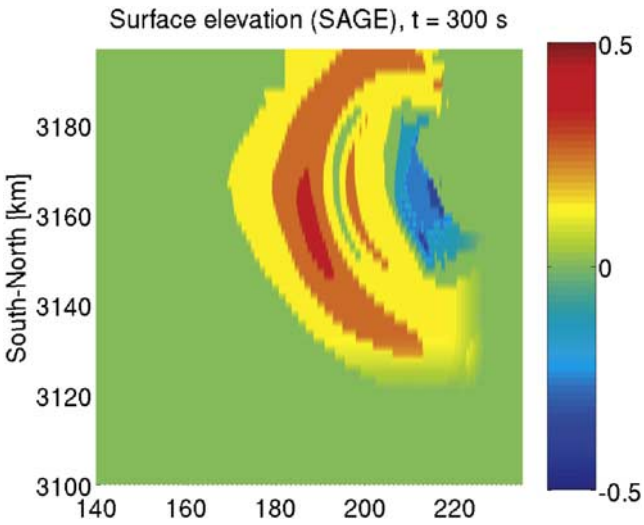

Figure 7. Surface elevation from SAGE at t = 300 s. The color bar gives the surface elevation in kilometers.

the minimum depths for the surrounding coastlines. The depth thresholds are varied according to their distance to La Palma Island, being 600 m for La Palma, 500 m for El Hierro, 200 m for La Gomera and Tenerife, and 100 m for Gran Canaria, Fuerteventura, Lanzarote, and Madeira. For the rest of the regional computational grid, the smallest depth allowed is 50 m. In subsequent, linear simulations we do not apply any such threshold.

[39] To check the accuracy, grid refinement tests were performed for a region covering longitudes 27.6°W–11.7°W and latitudes 21.7°N–36°N, using grid resolutions 0.5′, 1′ (interpolated from ETOPO 2) and 2′. The amplitude deviation and the L_2 norm of the leading wave are computed for different times along the two west-east transects shown in Figure 8, giving amplitude deviations that do not exceed 1.1% and 0.24% for the 2′ and 1′ grids respectively, thereby indicating convergence. The L_2 norms are invariably larger than the amplitude deviations (1–4% for the

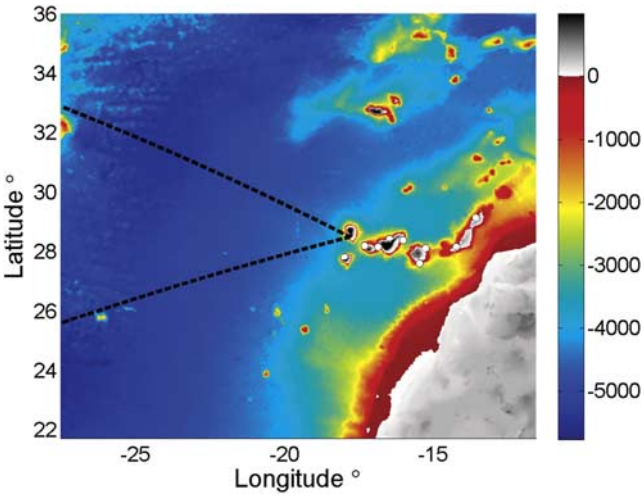

Figure 8. ETOPO 2 based computational domain for the Canary Islands simulations. The dashed lines indicate location of transects, whereas the white dots indicate time series locations.

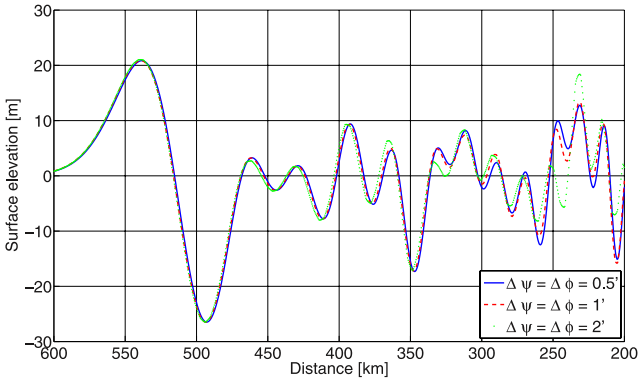

Figure 9. Surface elevation at t = 45 min for three different grid resolutions along the northern transect shown in Figure 8.

2′ grid, and 0.1–0.7% for the 1′ grid). Figure 9 shows that the leading wave is almost indistinguishable for different grid resolutions along the northern transect at t = 45 min, whereas the trailing waves deviate as the waves become shorter toward the rear of the displayed wave field. Because of contributions from the phase on the L_2 norm, L_2 norm deviations are much larger compared too L_{ampl}, pointing to the latter as a more convenient measure of the deviation. By inspecting the results for many transects and times, we find that the grid resolution of 2′ is good for the leading wave system for wavelengths >30 km. On the other hand, for wavelengths $\leq$30 km accuracy may vanish rapidly as exemplified in Figure 9. The subsequent analyses in the Canary Islands region are based on results on the 0.5′ grid.

5.2. Regional Wave Evolution

[40] After the landslide has entered the ocean, a sickle shaped wave with the main component moving in the south-west direction is generated, as shown in Figure 10. The wave is enormous, with surface elevations of more than 100 m and 50 m at distances of 100 km and 200 km west of La Palma Island respectively. A series of shorter trailing waves are following the leading wave. From Figure 10 it is evident that the waves propagating towards the east are smaller. Still, eastwards moving waves have maximum surface elevations of more than 20 m, thereby affecting all the Canary Islands severely.

[41] Figure 11 shows surface elevations compared with asymptotic scaling laws of $r^{-5/6}$, r^{-1}, and $r^{-7/6}$, along the northern and southern transects in Figure 8. Changes in η due to depth variations following Green's law of $\eta \propto h^{-1/4}$ are also included in the asymptotic scaling laws. Along both transects the decay rate of the wave front is between $r^{-5/6}$ and r^{-1} for the first 600 km of propagation. This yields a slightly slower relative attenuation than for the cylindrically symmetric simulations described in section 4.2. On the other hand, the 2HD results give smaller trailing waves for comparable distances.

[42] Next, we compute the directivity of the leading crest defining north as 90°, and south as −90° on the circle great circle of constant longitude $\psi = -17.9°$. A perpendicular great circle intersecting the other at latitudes $\phi = \pm 28.5°$, defines angles of 0° pointing southwest from La Palma towards the Lesser Antilles, and ±180° pointing correspond-

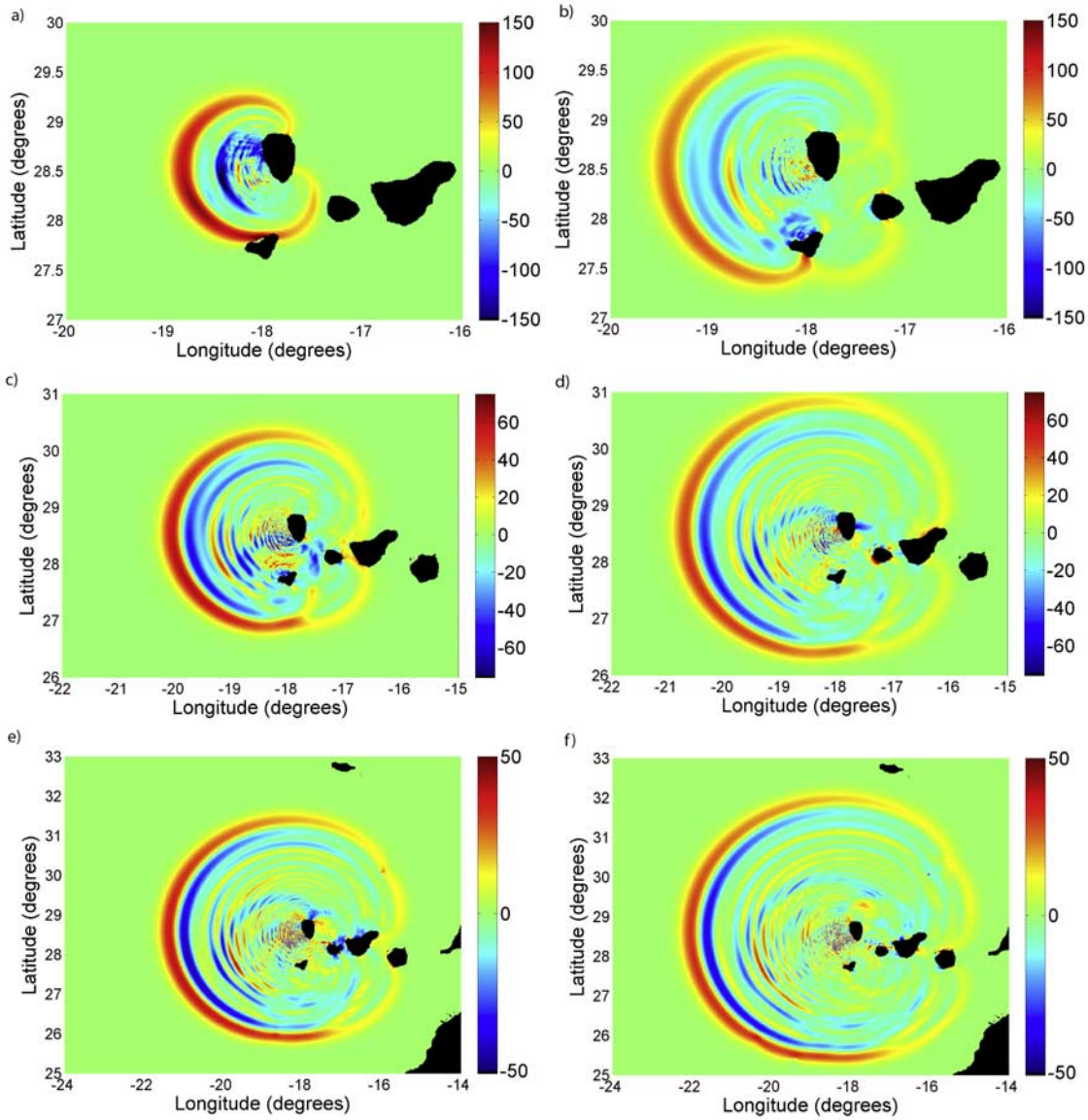

Figure 10. Simulated surface elevations using the standard Boussinesq model for (a) t = 10 min, (b) t = 15 min, (c) t = 20 min, (d) t = 25 min, (e) t = 30 min, and (f) t = 35 min.

ingly southeastwards. Figure 12 shows the locations and the directivity of the leading crest for propagation times up to 45 min. In the directivity plot, the surface elevations are normalized with respect to the maximum depth h_{max} = 5771 m using Green's law to reduce shoaling effects. The largest crests are found for an angle of approximately $-20°$ towards Suriname. However, the crest heights tend to be more evenly distributed with time. The leading crest decreases more or less monotonically as a function of angle, indicating that the diffraction effects are not dominating the early stages of propagation. However, the jump at an angle $\approx -75°$ is due to diffraction effects of the island of El Hierro.

5.3. Consequences in the Canary Islands

[43] Maximum surface elevations of the first crest for different time series are shown in Table 1. The surfaces elevations are in the range of 10–188 m, and give a rough impression of the potential disastrous consequences along the Canary Islands and close mainland regions. As stated previously we employ rigid walls at finite, and even large, depths in our Canary Island Boussinesq simulations. Such models, sometimes denoted as threshold models, leave out the last stage of shoaling, surf and runup on sloping beaches. They are often reported to underestimate runup [*Titov and Synolakis*, 1997, 1998]. Hence, the runup may be considerably larger than the tabulated near shore surface elevations, on the other hand, the slopes of the Canary Islands are steep, preventing large shoaling effects. At least, the computed maximum surface elevations in Table 1 are considered useful as they most likely provide lower limits of the runup.

[44] The largest impact would be caused by the slide itself and the huge runup of several hundred meters on northern La Palma. Also for the closest islands of El Hierro and La Gomera, Table 1 indicates that inundation may reach at least 188 m and 57 m respectively, thereby severely threatening all populated areas near shore, but also locations several km onshore. For example, flooding of the village of Frontera at

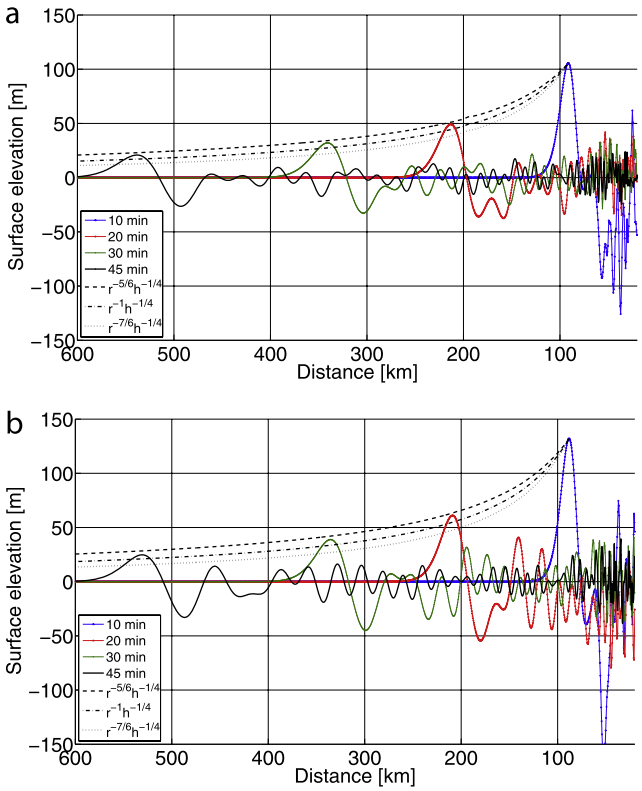

Figure 11. Surface elevations at different times. (a) Along the northern transect, and (b) the southern transect. The surface elevations are compared with analytical expressions combining radial spread, wave dispersion at the front, and Green's law.

El Hierro located at an elevation of 300 m above sea level cannot be ruled out, in addition, the numerous valleys of La Gomera would be inundated several km inland. Runup on Tenerife is expected to be largest along the west and north part of the Island, where the major tourist resorts are located. Although the surface elevations are smaller for the coastlines of Gran Canaria, Fuerteventura, and Lanzarote, Table 1 indicates that the wave amplitudes are still more than 10 m. It is noted that the two largest cities in the Canary Islands, Las Palmas and Santa Cruz, would be severely affected. Especially vulnerable is Las Palmas, where a large part of the city is located below the 20 m elevation.

6. Tsunami Propagation in the Atlantic Ocean

[45] For the 2HD simulations of the wave propagation across the Atlantic Ocean, we apply the linear dispersive model corresponding to equations (6) and (7) with $\epsilon = \gamma = 0$. The $2'$ computational grid was obtained using ETOPO 2 data (Figure 13), covering longitudes 90°W–0°W and latitudes 10°S–60°N. Initial surface elevation and velocities are extracted from the $0.5'$ Canary Islands simulations at t = 45 min.

[46] Numerical accuracy has been assessed through performing simulations, with and without the higher order numerical terms, both on the $2'$ grid and a coarser $4'$ grid. Errors may then be estimated both by assuming quadratic convergence for the simulations without numerical correction terms and by comparing the corrected and uncorrected methods. For the leading crest propagating across the ocean toward the west we find a numerical error in the uncorrected $2'$ simulation of approximately 1.5%. Naturally, the error in the best solution, obtained with higher order numerics and a $2'$ grid, is presumably much smaller. For the trailing waves the discrepancies are larger and display a more irregular evolution. For the six trailing crests the deviations between the corrected and uncorrected $2'$ simulations vary between 1% and 7%. This suggests that an error up to 5%, say, must be expected for the trailing waves in of the best solution. More details on the discretization errors are found in *Pedersen and Løvholt* [2008].

6.1. Transoceanic Wave Evolution

[47] Shortly after the wave has emerged from the Canary Islands, it is dominated by the first and second wave, as shown for t = 1 h 15 min in Figure 14. At t = 2 h 45 min, a dispersive wave train towards the southwest is clearly developed. At t = 5 h 45 min, the waves propagating westward approaches the coastlines of South America and

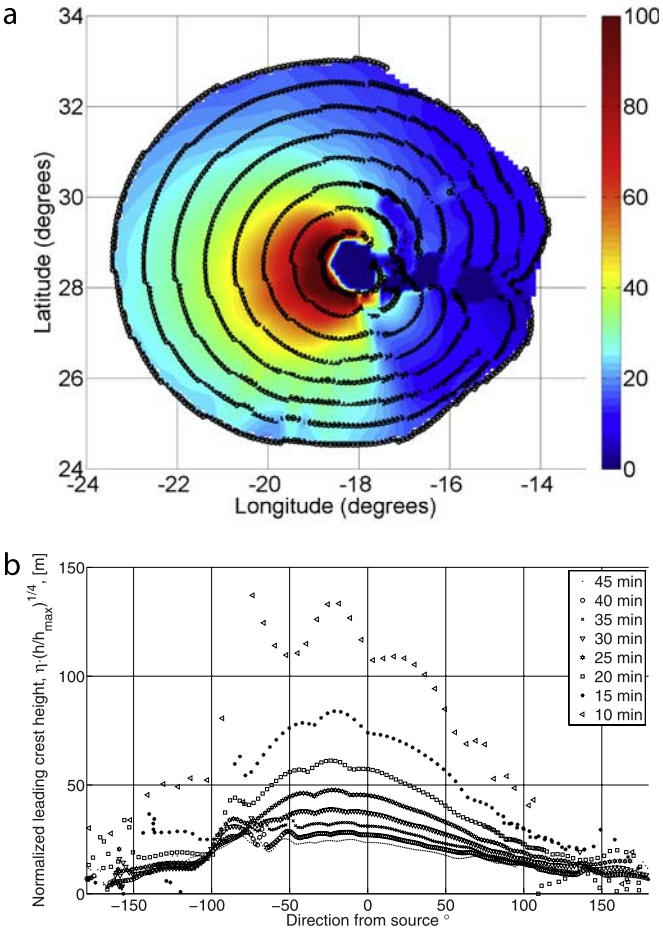

Figure 12. (a) Crest locations (lines) and interpolated heights at different times. (b) Leading crest heights normalized by the maximum depth h_{max} = 5771 m as a function of the direction. 90° points northwards and −90° points southwards along the longitude $\psi = -17.9°$, and 0° points towards the Lesser Antilles from La Palma Island.

Table 1. Maximum Surface Elevations and Depths for the First Crest for Different Time Series Locations[a]

Location	Water Depth	η_{max}
La Palma	runup	>300 m
El Hierro	1635 m	188 m
La Gomera	367 m	57 m
Tenerife North	506 m	32 m
Tenerife East	526 m	18 m
Tenerife West	603 m	47 m
Gran Canaria North	381 m	10 m
Gran Canaria South	695 m	10.5 m
Fuerteventura	396 m	13.6 m
Lanzarote	273 m	12.6 m

[a]The time series locations are given in Figure 8.

the Caribbean Islands, having dominating wave heights in the trailing system.

[48] To investigate the wave propagation in more detail, we again extract surface elevations at different times along the two transatlantic transects given in Figure 13 (extending the two in Figure 8), both being segments of great circles. First we find that the leading crest is predominantly largest along the northern transect in Figure 15. From the middle panel in Figure 14, we see that the sea-mounts south of the Azores generate a refraction pattern, which increases the amplitude in this region. After the shoals at about 2000 km, the leading wave decays more rapidly than the asymptotic solutions, most likely due to diffraction/refraction effects from sea-mounts and islands. In contrast to the evolution along the northern transect, the trailing waves have the largest amplitudes for most parts of the propagation along the southern transect. The leading crest decays as r^{-1}, whereas the the trailing crests decay with a rate more similar to $r^{-5/6}$. However, the latter displays larger fluctuations, indicating that interference effects play an important role throughout the transatlantic propagation. Both transects display large amplitudes of several meters before the waves enter the continental shelf; the largest amplitudes are directed towards the southwest.

[49] From the transoceanic transects, the wavelengths for the first four waves are found from the intervals between the zero crossings. For the leading wave, the wave-front is defined where the elevation equals a fraction of 0.1 times the leading crest. As shown in Figures 15 and 16, the wave system displays typical wavelengths ranging from 120–250 km for the leading wave, and 50–100 km for the first trailing waves, with the wavelength increasing as a function of distance. We compare the evolution of the wavelength with the asymptotic growth rate of $\lambda \propto r^{1/3}$ that arises from equations (11)–(12). A fairly good agreement is obtained for the overall characteristics of the leading wave along both transects. For both transects, a decrease in wavelength relative to the asymptotic solution are found over the mid-Atlantic ridge, as expected due to shoaling. The trailing waves display more disordered characteristics. The oscillations in λ for small r in Figure 15, are results of trailing waves with peaks below the zero sea level, i.e. at least 3/2 wavelengths are counted. It should also be kept in

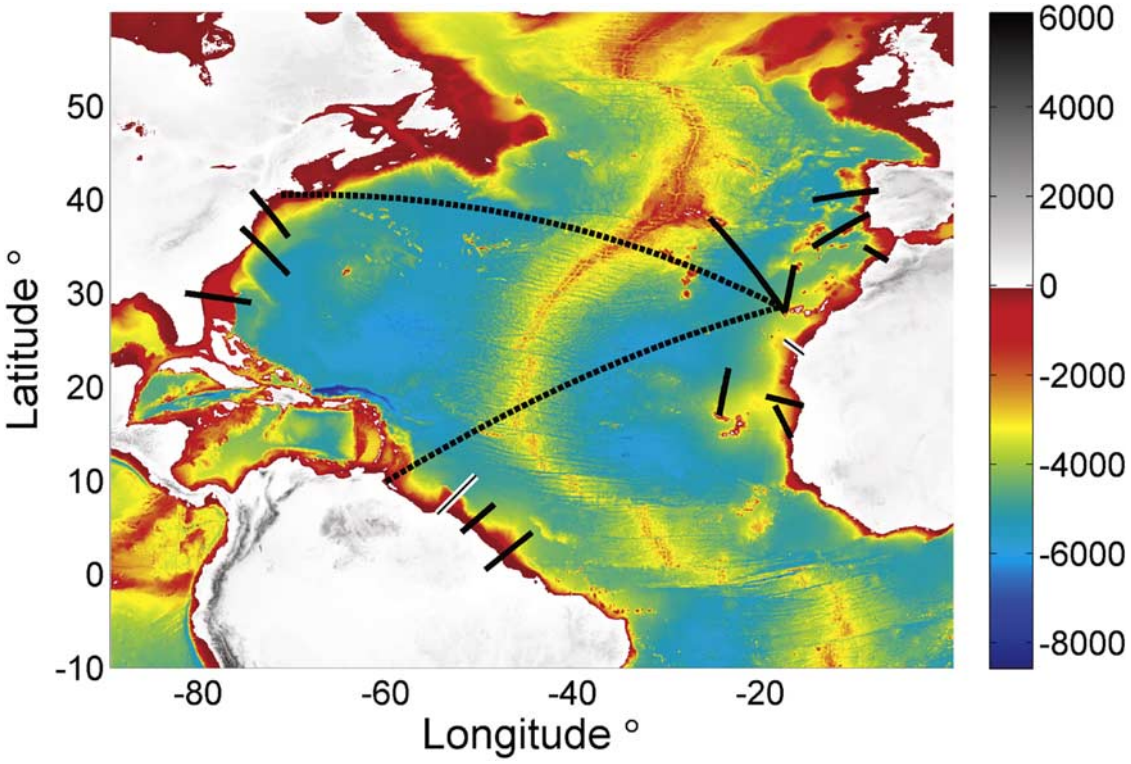

Figure 13. Computational domain for tsunami propagation over the Atlantic Ocean. The dashed lines indicate transects used for assessing asymptotic behavior of the waves. Solid lines indicate sections for investigation of near shore effects. The white and black solid lines near western Sahara and Suriname indicate transects where the wave evolution are visualized.

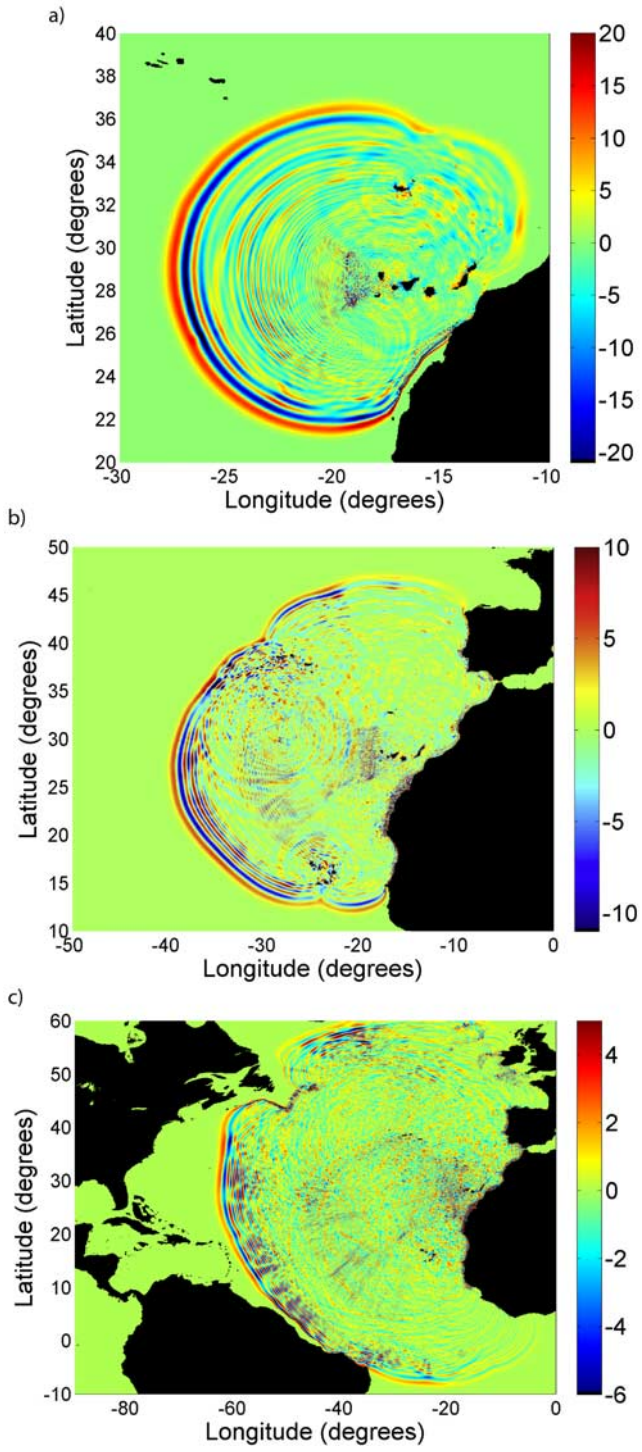

Figure 14. Simulated surface elevation after (a) 1 hour 15 min, (b) 2 hours 45 min, and (c) 5 hours 45 min.

mind that diffraction and refraction change the orientation of the waves, and as a consequence the wavelength measured over a transect is expected to be somewhat high if the propagation direction and transect are not parallel. This effect is particularly evident for the last part of propagation for the northern transect.

[50] Figure 17 shows the locations and the directivity of the leading crests for propagation times of 45 min to 4 h 15 min. The angles are computed as described in section 5.2. In the far field propagation the surface elevation as a function of direction is irregular owing to diffraction effects. The fluctuation of η as a function of direction is especially prominent towards northwest, as a result of strong diffraction/refraction from the Azores islands and nearby sea-mounts. Amplitudes are smaller in the directions normal to the slide motion, but the tendency is weaker than in the near field. However, it should then be kept in mind that for large propagation times, the largest amplitudes are found in the trailing waves. The trailing crests may not be studied similarly, as generally, only shorter segments are found as a result of diffraction, reflection and interference.

[51] The findings above show that the waves display a reasonable behavior within the range of different asymptotic theories. On the other hand, the simplified asymptotic solutions do not include the effects of diffraction and interference. In addition the source acts a mix of a dipole and monopole, even for transatlantic propagation.

6.1.1. Effects of the Earth's Rotation

[52] The effect of the Earth's rotation are important for long waves, that is, wavelengths comparable with the Rossby radius of deformation [*Gill*, 1982]. *Gill* [1982] gives a typical Rossby radius of ≈2000 km for depths of 4–5 km and 200 km for a depth of 40 m. These are considerably larger than the wavelengths found in the deep ocean in Figures 15 and 16 and near the shore in Figure 18, indicating small influence of the Earth's rotation.

[53] We quantify the importance of Coriolis forces on the far-field propagation across the Atlantic Ocean, along the two transoceanic transects given in Figure 13. The amplitude deviation for the leading crest at 6 h 45 min, for standard Boussinesq models with and without Coriolis terms, give 2.5% along the northern transect, and 1.5% along the southern transect. The leading waves are then still propagating on large depths.

6.2. Examples of Global Consequences

[54] Using the wavefield from the global grid as initial conditions, the wave propagation is simulated further in five regional domains with finer grid resolutions, as listed below. In this section, the results from the regional simulations are analyzed through bi-linear interpolation of the 2HD results to the near shore transects shown in Figure 13. Due to technical reasons, the basis of these simulations employed the linear dispersive model in the Canary Islands region. Compared to the simulations employing the Boussinesq model in the near field we find amplitude deviations of 2–7%, which are considered acceptable for the results presented below. However, due to these errors, the inaccuracies in the bathymetries that are interpolated from ETOPO-2 and omission of nonlinearities in regional domains, the results are admittedly only indicative. The five regional domains include: (1) Iberian peninsula and northern Morocco, $\Delta\psi$, $\Delta\varphi = 0.5'$. (2) Western Sahara, $\Delta\psi$, $\Delta\varphi = 0.5'$. (3) Mauritania, Senegal and Cape Verde, $\Delta\psi$, $\Delta\varphi = 0.67'$. (4) East coast of USA, $\Delta\psi$, $\Delta\varphi = 0.67'$. (5) Suriname, French Guyana, and northwestern Brazil, $\Delta\psi$, $\Delta\varphi = 1'$.

[55] The evolution of the incident waves are exemplified along the transects towards Western Sahara and Suriname in Figure 18. Both transects show waves of several meters height, with typical wavelengths of 100 km. Towards Western Sahara, the leading crest height is clearly exceeding

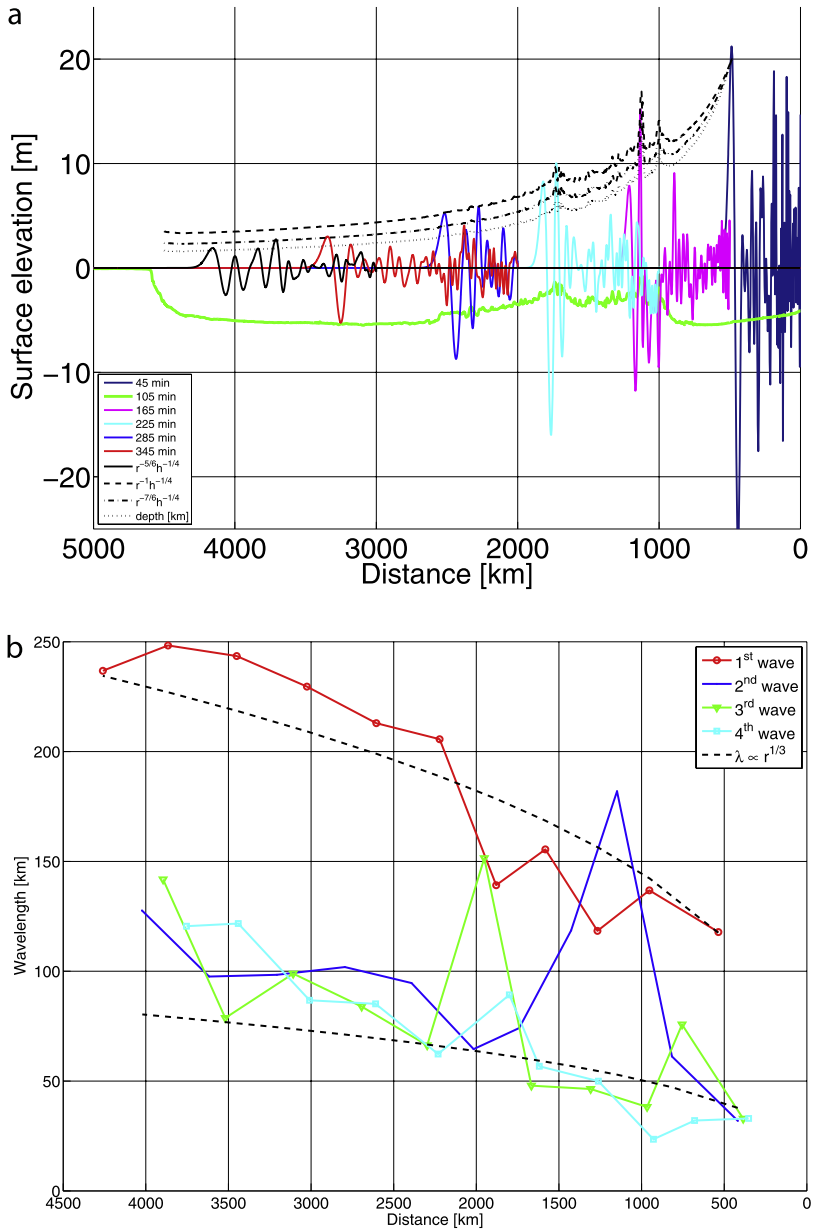

Figure 15. (a) Surface elevation at different times along the northern transatlantic transect given in Figure 13. Note that the tails of the wave-trains are removed for visibility. (b) First four wavelengths along the northern transoceanic transect.

the heights of the trailing crests, a typical example for the coastlines relatively near the Canary Islands (i.e. the Iberian Peninsula, northwestern Africa). In contrast, the incident waves towards Suriname consists of a series of large crests, where the trailing crests are higher than the the leading crest, a typical example for incident waves towards the American coastlines.

[56] To find comparable amplitudes for the transects shown in Figure 13 we normalize them by means of Green's law to a depth of 50 m, where the accumulated nonlinear effects generally have not yet influenced the amplitudes too strongly. We take care to employ Green's law from a transect profile at a time where the incident waves have attained a nearly normal incidence, the waves are still long enough to be properly resolved in the 2 min grid, the shoaling has made dispersive effects negligible and the wave pattern is unaffected by reflections from the shore. Moreover, we limit the study to the first few of the dominant incident crests. Naturally, in spite of all our precaution the procedure does only produce estimates of the incident waves. Reflections from the shore would sometimes have to be added to obtain the full surface elevation.

[57] Table 2 shows that the largest crest amplitudes are located close to the islands of Madeira and the Azores, however, it is noted that the tabulated values for the island locations including also Cape Verde, may exaggerate shoaling effects, as Green's law assumes normal incidence and gentle slopes. The table shows that the coastlines along Western Sahara are more severely affected than the coastlines than of Morocco. For the Iberian peninsula, and the coastlines

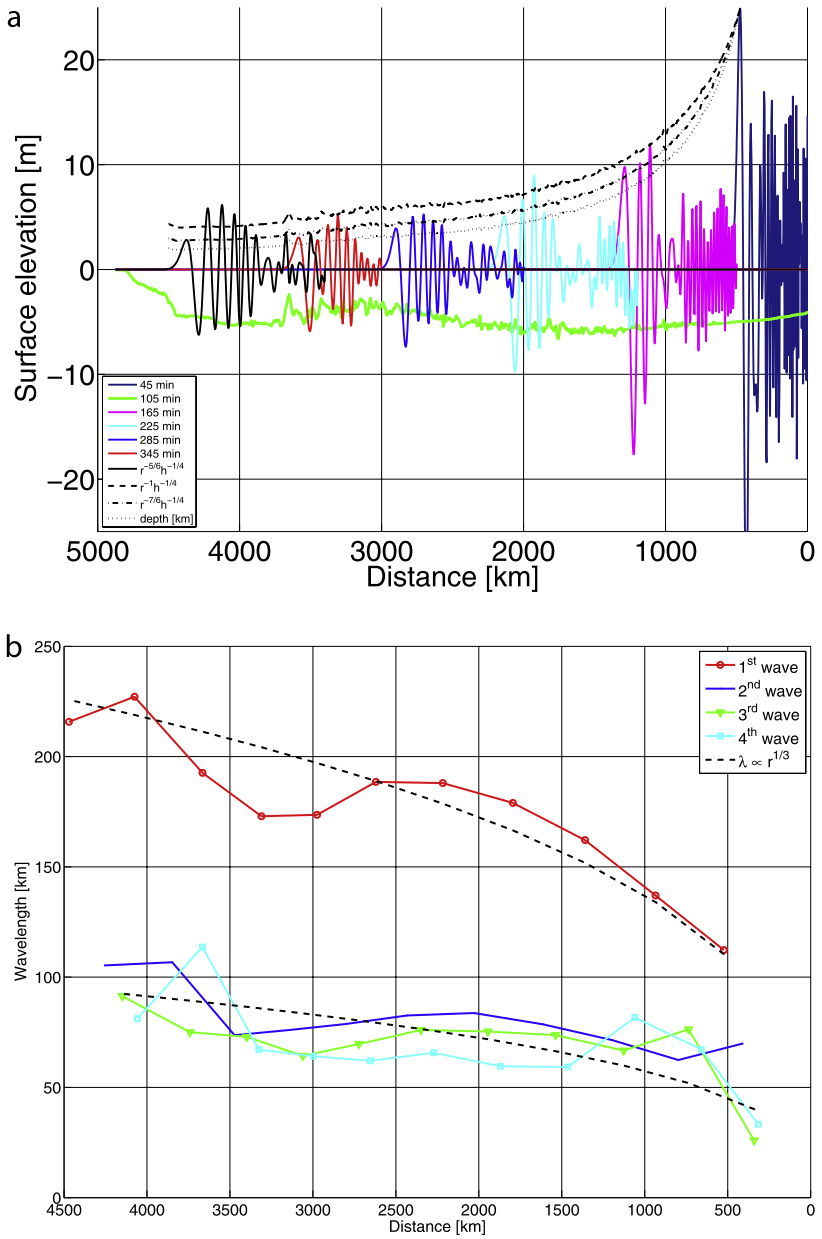

Figure 16. (a) Surface elevation at different times along the southern transatlantic transect given in Figure 13. Note that the tails of the wave-trains are removed for visibility. (b) First four wavelengths along the southern transoceanic transect.

of western Africa, the leading wave is largest. However, when the waves reach Cape Verde, the trailing waves have become larger than the leading one. The wave train incident on America is dominated by the trailing waves. As a result of a combination of the wave directivity and slow decay with distance, the incident amplitudes investigated in South America, exceed most of the amplitudes found in western Africa and on the Iberian peninsula. Along the coast of USA, we find amplitudes that are approximately a factor two smaller than for South America. Compared to the results of *Ward and Day* [2001], we find a maximum surface elevation that are 2–3 times smaller at the transect close to Florida. Still, Table 2 shows that the whole central part of the Atlantic Ocean would face severe consequences as result of the extreme scenario investigated here.

6.3. An Illustration of Continental Shelf Behavior

[58] The Atlantic coast of USA is fronted by an around 100 km wide shelf with depths less than 50 m. Incident on this shelf we have a sequence of wave crests with typical wavelengths in the order of hundreds of km and heights of several meters; with the leading wave being both smaller and longer than the following. In a simplified investigation of shoaling effects, simulations in a transect east-west, 36.2°N (off North Carolina) are performed. Initial conditions are extracted from the global simulation at t = 7 h 32 min, before the waves have entered the continental shelf. To capture the dynamics properly both nonlinearity and dispersion must be retained in the model. In addition a very fine resolution is needed. Still, the bathymetry is only

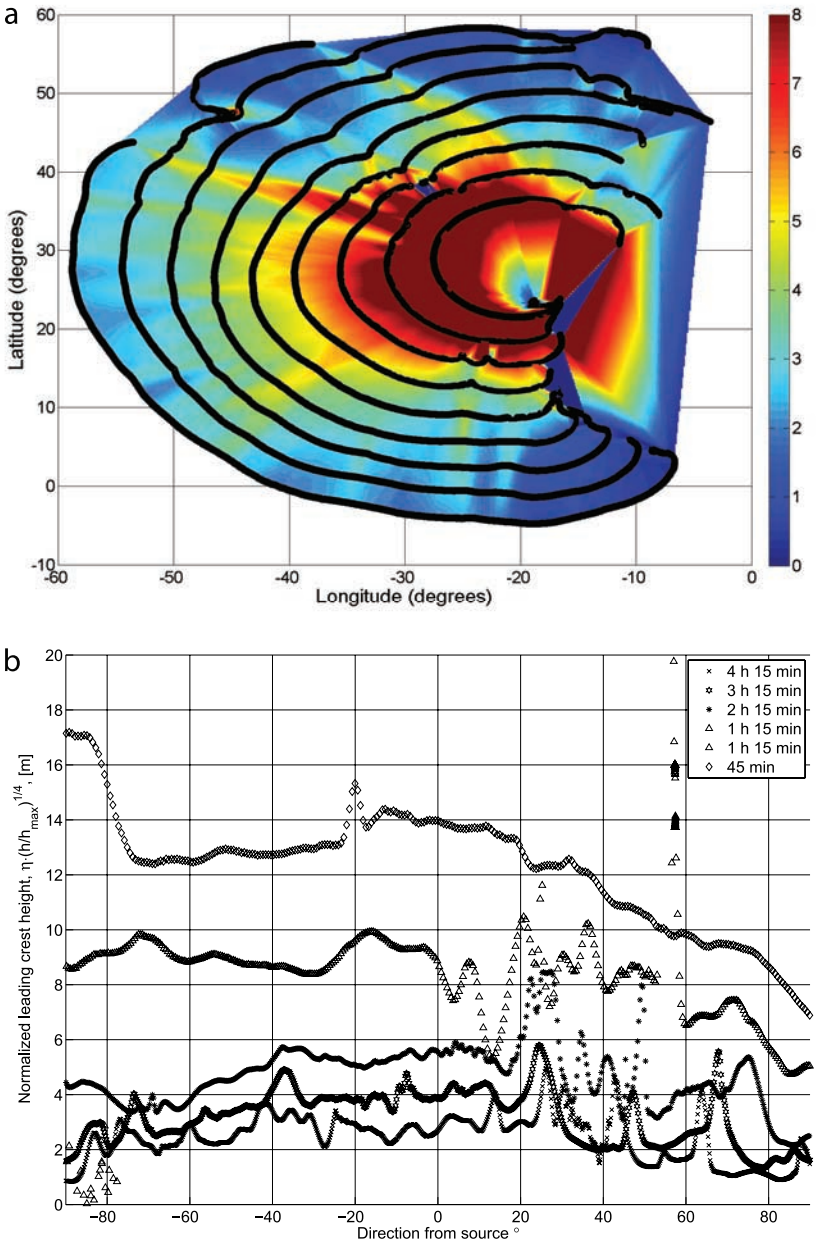

Figure 17. (a) Crest locations (lines) and interpolated heights for transoceanic propagation. (b) Leading crest heights normalized with the maximum depth h_{max} = 8637 m as a function of the direction. A 90° angle points northwards, and a −90° angle points southwards.

interpolated from the ETOPO-2. As a consequence of this, together with the lack of three-dimensional effects and the model limitations outlined below, the results in the current subsection should be regarded only as indicative of what might be expected on the continental shelf from an extreme La Palma event.

[59] As observed in Figure 19, upper two panels, the second crest rapidly evolves into an undular bore (sequence of solitary waves) at the continental shelf. The displayed results are produced with a model for plane waves employing a variable grid. The local Courant number is constant (near unity), for depths larger than a set minimum value, yielding $\Delta x \approx 4$ m for $h = 40$ m and $\Delta x \approx 40$ m in the deep ocean. For $t = 458$ min doubling the grid increments yields a change in the height and horizontal position of the maximum elevation (front of undular bore, see below) of 0.2 m and 8 m, respectively. The corresponding deviations for the leading crest (not yet a bore) are 10^{-5} m and 13 m, respectively. To obtain reasonably good results for the evolution of the individual peaks in Figure 19, mid panel, we need $\Delta x = 20$ m, say. A similar computation in two horizontal dimensions would thus have been very demanding.

[60] At $t = 458$ min a large number of crests have evolved and the elevation of the leading one has reached 26.5 m, which corresponds to a wave height of 39 m measured from the toe (depth of through 12.5 m). Taking into account the

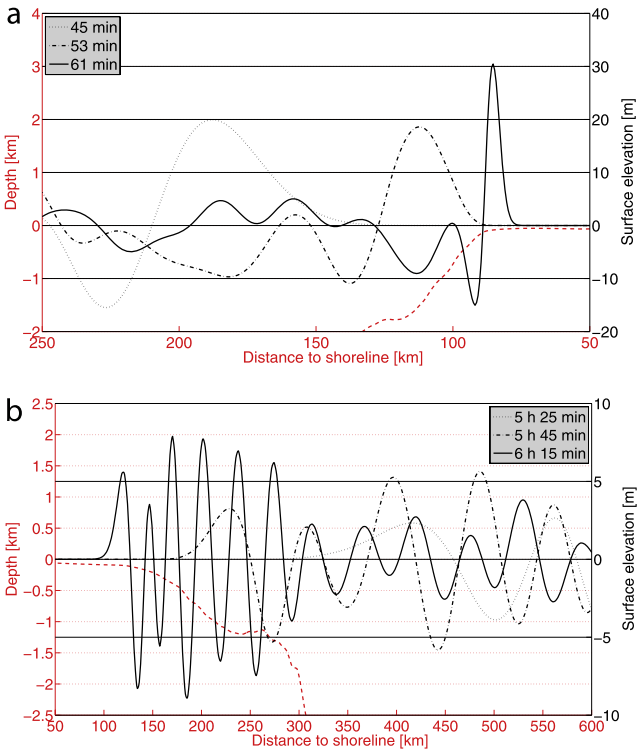

Figure 18. (a) Wave evolution along a transect towards western Africa, and (b) towards Suriname. Note the difference in scale. The dashed lines indicate the depth.

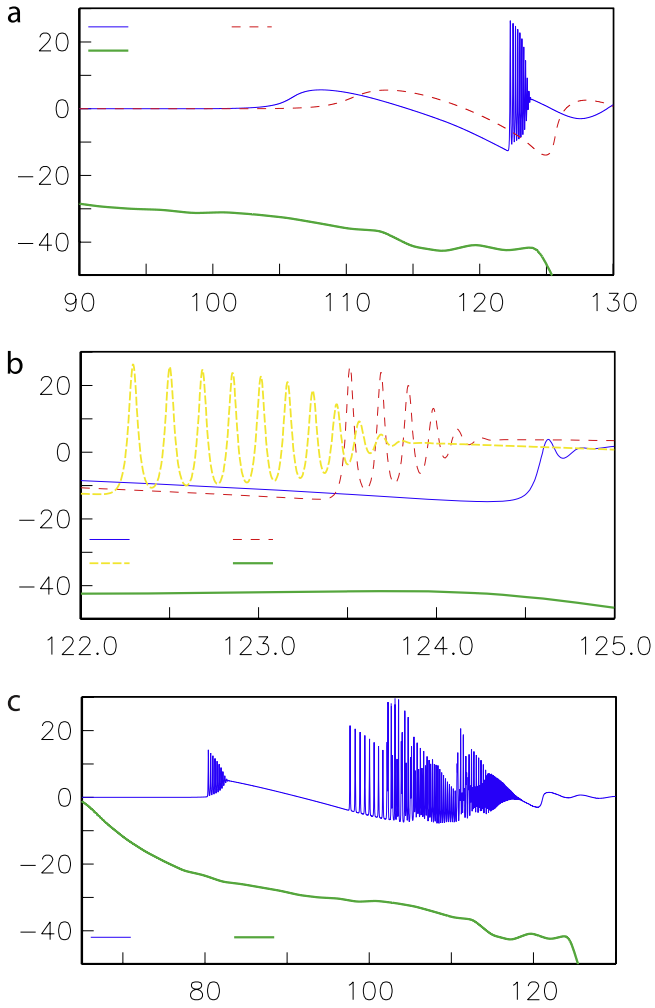

Figure 19. Surfaces marked by time in minutes. (a) Evolution of bore from second incident elevation; (b) blow-up of evolution; (c) disintegration of more incident waves.

equilibrium depth of approximately $h = 42.4$ m the height of the leading crest corresponds to a local solitary wave amplitude larger than the depth. This is outside the validity of a weakly nonlinear Boussinesq model, such as the one employed here, and also clearly above the stability limit for a solitary wave of elevation 0.72 times the depth [*Kataoka and Tsutahara*, 2004]. The waves are already breaking. At the instant where the first peak, and thereby the undular bores, starts to develop (not shown) the the ratio between wave-height (trough to peak) and depth is about 0.35. In constant depth this is close to the upper limit of a non-breaking undular bore, in the sense that the expected doubling of the wave-height [*Peregrine*, 1966] nearly corresponds to the stability limit for solitary waves given above. When the shoaling is taken into consideration the bore will probably best be regarded as an intermediate case between a traditional breaking bore and a breaking undular

Table 2. Examples of Crest Amplitudes of Incident Waves Along Transects, Also Normalized to a Depth of 50 m by Green's Law[a]

Location	h_{lead}	h_{max}	η_{lead}	η_{max}	$\eta_{50,lead}$	$\eta_{50,max}$	No. max
Portugal North	66 m	66 m	7.3 m	7.3 m	7.8 m	7.8 m	1st
Portugal South	1550 m	1550 m	3.0 m	3.0 m	7.1 m	7.1 m	1st
Morocco	90 m	90 m	4.3 m	4.3 m	5.5 m	5.5 m	1st
Western Sahara	55 m	55 m	37 m	37 m	37 m	37 m	1st
Mauritania	106 m	106 m	9.7 m	9.7 m	11.7 m	11.7 m	1st
Senegal	378 m	378 m	8.4 m	8.4 m	13.9 m	13.9 m	1st
Cape Verde*	2.96 km	3.53 km	8.2 m	11.3 m	23 m	33 m	3rd
Madeira*	3.68 km	3.68 km	13.7 m	13.7 m	40 m	40 m	1st
Azores*	4.24 km	4.24 km	9.6 m	9.6 m	29 m	29 m	1st
Suriname	98 m	850 m	5.6 m	7.7 m	6.6 m	15.7 m	4th
French Guyana	71 m	91 m	5.9 m	12.7 m	6.4 m	14.7 m	4th
Northern Brazil	73 m	81 m	7.4	13.6 m	8.1 m	15.3 m	2nd
USA South	840 m	5.0 km	2.2 m	3.0	4.5 m	9.5 m	4th
USA Mid	33 m	60 m	5.7 m	9.6 m	5.2 m	10.0 m	2nd
USA North	43 m	43 m	4.8 m	4.8 m	4.6 m	4.6 m	1st

[a]Both amplitudes for the leading crests η_{lead} as well as the maximum crests η_{max} are shown, the abbreviations $\eta_{50,lead}$, $\eta_{50,max}$, correspond to normalized quantities. The crest number corresponding to the maximum is included, so is also the depth corresponding to the given amplitudes. The asterisk denotes that the transects ends near an island.

bore. The breaking will then affect the interaction of the individual peaks that is involved in the fission and thereby the evolution of the bore as a whole. For individually breaking solitary-like waves gradient dependent diffusion have been employed with some success [*Kennedy et al.*, 2000; *Lynett et al.*, 2002; *Lynett*, 2006] but, to the authors knowledge, no theoretical study on the evolution of breaking undular bores is published. Such a study is beyond the scope of this article.

[61] Before $t = 470$ min also the first crest is transformed to an undular bore. Ten minutes later (Figure 19, lower panel) the disintegration of the leading wave is significant with an amplitude of the leading crest of 14.3 m which is around 0.6 times the local depth. This wave may not be breaking yet, but is somewhat high for the standard Boussinesq equations. For bores of similar heights, *Wei et al.* [1995] found that standard Boussinesq models gave noticeable errors, but still qualitatively correct behavior. However, in mildly shoaling water solitary waves amplify in inverse proportion to the depth [*Miles*, 1980; *Glimsdal et al.*, 2007], which is faster than periodic waves. Hence, also the solitary waves from this bore will rapidly surpass the breaking limit. More analysis would have been required before any assessment can be made on the consequences for coastal impact and inundation. On one hand the evolution of the undular bore roughly doubles the wave height. On the other hand, a series of breaking individual peaks may lead to more substantial energy loss than traditional breaking tsunami-bores. In addition the waves, evolving from the solitary waves, that do reach the shoreline may also have a reduced potential for long inundation due their short wavelengths. At $t = 470$ min the trailing incident crests that have entered the continental shelf (2 through 4) have all been consumed by the undular bore dynamics to yield series of high solitary waves. However, for incident waves 2–4 the solution must be regarded as formal because of the high amplitudes.

[62] Undular bores due to tides are regularly observed in some estuaries and rivers and have sometimes been reported for tsunamis as well [*Shuto*, 1985]. Recently, undular bores have been discussed in relation to the propagation of the 2004 Indian Ocean tsunami in the Malacca Strait [*Glimsdal et al.*, 2006; *Grue et al.*, 2008].

[63] Undular bores are not inherent in the NLSW models and many tsunami modelers are unaware of the phenomenon or do not appreciate its significance. We believe that this is one aspect where standard modeling practice, based on the NLSW equations, differs from reality.

7. Concluding Remarks

[64] In this paper, we have performed simulations of the wave generation and propagation due to a potential landslide from the La Palma island, based on the work of *Gisler et al.* [2006]. Although the probability of this extreme scenario is considered small, the potential catastrophic consequences call for attention. Moreover, it is a large scale event, requiring multimaterial fully nonlinear models in the near-field, and dispersive models in the far-field; such models are seldom used for the global extents encountered herein.

[65] The combined slide motion and tsunami generation are modeled with the multimaterial model SAGE in both a cylindrical symmetric and a three-dimensional geometry. The maximum slide speed is close to critical, thereby effectively generating a large leading wave. The main wave direction is southwestwards, pointing towards the northwestern part of South America. As the wave propagates away from the generation area, we show that by transferring the SAGE data to a numerical Boussinesq model, the continued propagation into the far-field is successfully simulated. Moreover, more standard tools as the LSW and NLSW models should not be used, as dispersion is important for the wave propagation. However, inclusion of dispersion to the first order is sufficient for the describing the wave propagation, and higher order models, such as the one of *Nwogu* [1993], are not needed.

[66] A cylindrically symmetric model is used to investigate the far field characteristics of the wave-system, giving a decay close to r^{-1} for the leading wave. A stable asymptotic state is not reached for the trailing waves as a result of interference, even for propagation distances comparable to half the circumference of the Earth. In the 2HD model for the Atlantic Ocean we identify similar characteristics for the evolution of the wavefield. However, directivity, diffraction, refraction, and shoaling combined with dispersion leads to a complex wave-system, and asymptotic scaling laws are not describing the far-field propagation accurately. In fact, constructive interference is shown to effectively reduce the decay of the trailing waves with distance compared to asymptotic theory.

[67] By using a 2HD Boussinesq model formulated in geographical co-ordinates, we simulate the wave field close to the Canary Islands as well as for the central Atlantic Ocean. Examples of lower limits of the possible consequences due to the scenario are briefly monitored by investigating the near shore wave evolution using time series and transects. In the near field, the leading wave causes the largest surface elevations, whereas as series of large waves, dominated by the first 2–6 trailing waves, are found for transatlantic propagation distances. In the Canary Islands, we find maximum surface elevations in the 10–188 m range for depths between 273 m and 1635 m. Outside the Canary Islands, large surface elevations up to 40 m are found in the closest island systems and in western Sahara. We also find that the largest surface elevations seen off the American coast are larger than most of those at the coasts of Portugal and Africa. Compared to previous simulations of the La Palma scenario, we find smaller surface elevation than *Ward and Day* [2001], but larger than the findings of *Mader* [2001]. We believe that this paper represents a qualitatively improved picture of the dynamics of the extreme scenario, as we include the full 3-D representation of the the wave generation, a full numeric treatment of the 2HD dispersive wave propagation in combination, and explore the nature of the wave propagation in more detail.

[68] Finally, we note that the examples of near-shore wave evolution are investigated in 1HD by using a Boussinesq model for a transect towards North Carolina. Then, a series of undular bores are developed, in turn leading to a strong increase of surface elevations. It is emphasized the individual crests of the undular bores generally break far off shore and that effects of this breaking on the dynamics on the undular bores itself are not modeled. Still, it is clear that breaking will counteract the extra amplification due to the undular bore.

[69] Several features explored in this paper are not commonly encountered in standard investigations of tsunami propagation and propagation. These features include a fully nonlinear treatment of the multiphase flow of the rock, water and air; transoceanic dispersive wave propagation; and the evolution of undular bores. As shown, the combination of all these effects is in fact necessary to explain the wave dynamics. Modelers should also be aware of the complexity in the radiation pattern due to dispersion, and that both the NLSW models commonly used for transoceanic propagation, and asymptotic analytical solutions may fail to describe the propagation to the far-field.

Appendix A: Numerical Methods in SAGE

[70] SAGE runs in several geometries: one-dimensional Cartesian and spherical, two-dimensional Cartesian and cylindrical symmetry, and three-dimensional Cartesian. Because modern supercomputing is often performed on clusters of many identical processors, the parallel implementation of the code is supremely important. For portability and scalability, SAGE uses the widely available MPI (message passing interface). Load leveling is accomplished through the use of an adaptive cell pointer list, in which newly created daughter cells are placed immediately after the mother cells. Cells are redistributed among processors at every time step, while keeping mothers and daughters together. With M cells and N processors, this gives roughly M/N cells per processor, for good load balancing. As neighbor-cell variables are needed, the message passing interface−gather/scatter routines copy those neighbor variables into local scratch.

[71] For second-order accuracy in time (except at shocks), the method in the SAGE is a hybrid that advances by an intermediate Lagrangian half-step to compute the correct Eulerian fluxes at the cell faces. The advance for the full time step is then performed by solving the Riemann problem for the characteristics using the cell-face half-time-step fluxes. Care is taken in the advancement scheme and in the refinement step to preserve conservation of mass, momentum, and energy. The SAGE code and its descendant RAGE (which incorporates radiation transport) have been subjected to extensive verification and validation studies. These studies and more details on the hydrodynamic method are given in *Gittings et al.* [2006].

[72] The cells in the Eulerian grid are subdivided when gradients in material properties exceed a threshold, down to minimum sizes specified by the user for each material separately for bulk and interfaces. Since each cell can contain many materials, partial stresses are calculated from the constitutive relations and combined according to the assumption of local thermodynamic equilibrium within the cell.

Appendix B: Numerical Method for the Boussinesq Equations

[73] The finite difference method for solving the set (6) and (7) is developed from the model employed and documented in *Pedersen and Rygg* [1987] and *Rygg* [1988]. As opposed to these references we discretize a somewhat different formulation of the Boussinesq equations and include effects related to the curvature and rotation of the Earth. Most of the computer code is rewritten. Like a number of shallow water models, as well as a few Boussinesq models, such as *Beji and Nadaoka* [1996] and *Shi et al.* [2001], we employ the staggered C-grid [*Mesinger and Arakawa*, 1976] in the spatial discretization. Unlike *Beji and Nadaoka* [1996] and *Shi et al.* [2001], but similar to many hydrostatic models, we employ a staggered grid also in time with nodes for surface elevation and velocities alternating along the time axis.

[74] We will not spell out the discrete equations herein, but refer to the accompanying technical report [*Pedersen and Løvholt*, 2008] for details. Instead we observe the following key points:

[75] 1. Owing to the staggered grid, in space and time, we may replace all the linear derivatives in (6) and (7) by symmetric, centered differences. This yields a more accurate temporal resolution than *Beji and Nadaoka* [1996] and a much simpler time stepping procedure than the multilevel predictor/corrector method employed in the FUNWAVE [*Kirby et al.*, 1998; *Kirby*, 1998; *Shi et al.*, 2001] and COULWAVE [*Lynett and Liu*, 2004] models. In the nonlinear terms, the Coriolis term and coefficients we also employ symmetric averaging.

[76] 2. Numerical correction terms are included to obtain a fourth order method for the dominant LSW balance ($\mu, \epsilon \rightarrow 0$) of the equations. In some respects these resemble the higher order spatial differences in FUNWAVE, but for the present model we must include temporal corrections as well. However, due to the staggered grid and the one-level temporal scheme the corrections must be re-casted by means of the leading order balance of the Boussinesq equations. This results in additional discrete terms akin to the dispersion terms normally appearing in Boussinesq type equations. In the forerunner model [*Pedersen and Rygg*, 1987; *Rygg*, 1988] a similar procedure was applied to obtain an improved numerical dispersion relation, but not a full fourth order scheme for the LSW part of the Boussinesq equations. In their related model *Beji and Nadaoka* [1996] did not include higher order numerical representations.

[77] 3. When nonlinearity and dispersion are retained, both the continuity and momentum equations yield implicit sets of equations to be solved at every time steps. The temporally staggered grid allows the implicit continuity equation set to be decoupled from momentum equation sets. Naturally, exact volume conservation is observed in the equation of continuity.

[78] 4. Geometrical averaging is used in the convective term to obtain linear implicit sets from the momentum equation. The resulting discrete Boussinesq equations are nondissipative and inherit nonattenuating discrete solitary-wave solutions [*Pedersen*, 1991]. Such a property may not be obtained when asymmetric differences are used. On the other hand, the model in its present form is particularly adapted to long distance propagation of linear or nonbreaking waves. If breaking is to be included, other nonlinear discretizations may be more favorable.

[79] 5. One of the crucial operations in Boussinesq type models is the iteration applied at each time step to the momentum equations. We have adapted the ADI (alternating direction implicit) iteration from the models predecessors [*Pedersen and Rygg*, 1987; *Rygg*, 1988]. In the present context this implies alternating implicit sweeps in the x and

y components of the momentum equation, similar to the approach of *Beji and Nadaoka* [1996]. The iteration scheme is much simpler than, for instance, the one used in the FUNWAVE and COULWAVE models and two sweeps do suffice for the present application [*Pedersen and Løvholt*, 2008]. For cases dominated by shorter waves, the number of iterations would have to be increased.

[80] 6. Runup on sloping beaches and breaking are not yet included and land is represented as staircase, no-flux boundaries. Such boundaries have been shown to function well, even in the nonlinear case, when situated in water of sufficient depth [*Pedersen and Løvholt*, 2008]. On the other hand, dry cells during withdrawal cause problems and may not be permitted. At open boundaries we employ sponge layers.

[81] 7. No smoothing is applied to the computed surfaces and velocities as such. An optional number of five points smoothings may be applied to the dispersion optimization terms ($\gamma \neq 0$) and the higher order numerical correction terms. No smoothing was required for the applications reported herein.

[82] **Acknowledgments.** We are indebted to Peter Gauer, Carl B. Harbitz, and Sylfest Glimsdal for their helpful comments. We also thank two anonymous referees and Associate Editor James Kirby for comments that significantly improved the quality of the paper. This work has been supported by the Research Council of Norway under grant 154831, by the International Centre for Geohazards (ICG), and by the Norwegian Geotechnical Institute (NGI). The present article is contribution 202 of the International Centre for Geohazards.

References

Abadie, S., S. Grilli, and S. Glockner (2006), A coupled numerical model for tsunamis generated by subarial and submarine mass failures, in *30th Conference on Coastal Engineering*, pp. 1420–1431.

Bardet, J.-P., C. Synolakis, H. Davis, F. Imamura, and E. Okal (2003), Landslide tsunamis: Recent findings and research directions, *Pure Appl. Geophys.*, *160*, 1793–1809.

Beji, S., and K. Nadaoka (1996), A formal derivation and numerical modelling of the improved Boussinesq equations for varying depth, *Ocean Eng.*, *23*(8), 691–704.

Bondevik, S., F. Løvholt, C. Harbitz, J. Mangerud, A. Dawson, and J. Svendsen (2005), The Storegga slide tsunami comparing field observations with numerical simulations, *Mar. Pet. Geol.*, *22*, 195–208.

Bryn, P., K. Berg, C. Forsberg, A. Solheim, and T. Kvalstad (2005), Explaining the Storegga slide, *Mar. Pet. Geol.*, *22*, 11–19.

Bugge, T., R. Belderson, and N. Kenyon (1988), The Storegga slide, *Philos. Trans. R. Soc. London, Ser. A*, *325*, 357–398.

Carracedo, J., S. Day, H. Guillou, and P. Gravestock (1999), Later stage of volcanic evolution of La Palma, Canary Islands: rift evolution, giant landslides, and the genesis of the Caldera de Taburiente, *Bull. Geol. Soc. Am.*, *111*, 755–768.

Elverhøi, A., D. Issler, F. De Blasio, T. Ilstad, C. Harbitz, and P. Gauer (2005), Emerging insights into the dynamics of submarine debris flows, *Nat. Hazards Earth Syst. Sci.*, *5*, 633–648.

Fine, I., A. Rabinovich, B. Bornhold, R. Thomson, and E. Kulikov (2005), The Grand Banks landslide-generated tsunami of November 18, 1929: Preliminary analysis and numerical modelling, *Mar. Geol.*, *215*, 45–57.

Fritz, H., W. H. Hager, and H.-E. Minor (2003a), Landslide generated impulse waves. 1. Instantaneous flow fields, *Exp. Fluids*, *35*, 505–519.

Fritz, H., W. H. Hager, and H.-E. Minor (2003b), Landslide generated impulse waves. 2. Hydrodynamic impact craters, *Exp. Fluids*, *35*, 520–532.

Fritz, H., W. H. Hager, and H.-E. Minor (2004), Near field characteristics of landslide generated impulse waves, *J. Waterw. Port Coastal Ocean Eng.*, *130*(6), 287–302.

Garcia, M. O. (1996), Turbidites from slope failure on Hawaiian volcanoes, in *Volcano Instability on the Earth and Other Planets*, vol. 110, edited by W. McGuire, A. Jones, and J. Neuberg, pp. 281–294, Geol. Soc., London, UK.

Gauer, P., T. Kvalstad, C. Forsberg, P. Bryn, and K. Berg (2005), The last phase of the Storegga slide: simulation of retrogressive slide dynamics and comparison with slide-scar morphology, *Mar. Pet. Geol.*, *22*, 171–178.

Gill, A. (1982), *Athmosphere-Ocean Dynamics*, *Int. Geophys. Ser.*, vol. *30*, Academic, San Diego, Calif.

Gisler, G. (2008), Tsunami generation - Other sources, in *The Sea*, vol. 15, Harvard Univ. Press, Cambridge, Mass., in press.

Gisler, G., R. Weaver, and M. Gittings (2006), SAGE calculations of the tsunami threat from La Palma, *Sci. Tsunami Hazards*, *24*, 288–301.

Gittings, M. L., et al. (2006), The RAGE radiation-hydrodynamic code, *Los Alamos Unclassified Rep. LA-RU-06-0027*, Los Alamos Natl. Lab., Los Alamos, N. M.

Glimsdal, S., G. Pedersen, K. Atakan, C. B. Harbitz, H. Langtangen, and F. Løvholt (2006), Propagation of the Dec. 26, 2004 Indian Ocean Tsunami: effects of dispersion and source characteristics, *Int. J. Fluid Mech. Res.*, *33*(1), 15–43.

Glimsdal, S., G. Pedersen, H. Langtangen, V. Shuvalov, and H. Dypvik (2007), Tsunami generation and propagation from the Mjølnir asteroid impact, *Meteorit. Planet. Sci.*, *42*, 1473–1493.

Grilli, S. T., and P. Watts (2005), Tsunami generation by submarine mass failure. I: Modelling, experimental validation, and sensitivity analyses, *J. Waterw. Port Coastal Ocean Eng.*, *131*(6), 283–297.

Grue, J., E. N. Pelinovsky, D. Fructus, T. Talipova, and C. Kharif (2008), Formation of undular bores and solitary waves in the Strait of Malacca caused by the 26 December 2004 Indian Ocean tsunami, *J. Geophys. Res.*, *113*, C05008, doi:10.1029/2007JC004343.

Hampton, M., H. Lee, and J. Locat (1996), Submarine landslides, *Rev. Geophys.*, *34*, 33–59.

Harbitz, C. B. (1992), Model simulations of tsunamis generated by the Storegga slides, *Mar. Geol.*, *105*, 1–21.

Heezen, B., and M. Ewing (1952), Turbidity currents and submarine slumps, and the 1929 Grand Banks Earthquake, *Am. J. Sci.*, *250*, 775–793.

Imran, J., G. Parker, J. Locat, and H. Lee (2001), 1-d numerical model of muddy subaqueous and subaerial debris flows, *J. Hydrol. Eng.*, *127*, 959–968.

Ioualalen, M., J. Asavanant, N. Kaewbanjak, S. T. Grilli, J. T. Kirby, and P. Watts (2007), Tsunami generation by submarine mass failure: 1. Modeling, experimental validation, and sensitivity analyses, *J. Geophys. Res.*, *112*, C07024, doi:10.1029/2006JC003850.

Jiang, L., and P. LeBlond (1992), The coupling of a submarine slide and the surface waves which it generates, *J. Geophys. Res.*, *97*, 731–744.

Kataoka, T., and M. Tsutahara (2004), Transverse instability of surface solitary waves, *J. Fluid Mech.*, *512*, 211–221.

Kennedy, A. B., Q. Chen, J. T. Kirby, and R. A. Dalrymple (2000), Boussinesq modeling of wave transformation, breaking, and run-up. Part I: 1D, *J. Waterw. Port Coastal Ocean Eng.*, *126*(1), 39–47.

Kirby, J. T. (1998), Funwave software download page. (Available at http://chinacat.coastal.udel.edu)

Kirby, J. T., G. Wei, Q. Chen, A. B. Kennedy, and R. A. Dalrymple (1998), Fully nonlinear Boussinesq wave model documentation and user's manual, *Research Rep. CACR-98-06*, Cent. for Appl. Coastal Res., Dep. of Civ. Eng., Univ. of Delaware, Newark. (Available at http://chinacat.coastal.udel.edu)

Kirby, J. T., F. Shi, P. Watts, and S. T. Grilli (2004), Propagation of short, dispersive tsunami waves in ocean basins, *Eos Trans. AGU*, *85*(47), Fall Meet. Suppl., Abstract OS21-E02.

Krastel, S., H. Schminke, C. Jacobs, T. Le Bas, and B. Alibés (2001), Slope landslides around the Canary Islands, *J. Geophys. Res.*, *106*, 3977–3997.

Liu, P.-F., T.-R. Wu, F. Raichlen, C. Synolakis, and J. Borrero (2005), Runup and rundown generated by three-dimensional sliding masses, *J. Fluid Mech.*, *536*, 107–144.

Locat, J., and H. Lee (2002), Submarine landslides: Advances and challenges, *Can. Geotech. J.*, *39*, 193–212.

Lynett, P. J. (2006), Nearshore wave modeling with high-order Boussinesq-type equations, *J. Waterw. Port Coastal Ocean Eng.*, *132*(5), 2119–2146.

Lynett, P. J., and P. L.-F. Liu (2004), Coulwave model page. (Available at http://ceprofs.tamu.edu/plynett/COULWAVE/default.htm)

Lynett, P. J., T.-R. Wu, and P. L.-F. Liu (2002), Modeling wave runup with depth-integrated equations, *Coastal Eng.*, *46*, 89–107.

Lynett, P. J., J. C. Borrero, P. L.-F. Liu, and C. E. Synolakis (2003), Field survey and Numerical Simulations: A review of the 1998 Papua New Guinea Tsunami, *Pure Appl. Geophys.*, *160*, 2119–2146.

Mader, C. (1999), Modelling of the 1958 Lituya Bay mega-tsunami, *Sci. Tsunami Hazards*, *17*(2), 57–67.

Mader, C. (2001), Modeling the La Palma Island tsunami, *Sci. Tsunami Hazards*, *19*(3), 150–170.

Mader, C. (2004), *Numerical Modelling of Water Waves*, 2nd ed., CRC Press, Boca Raton, Fla.

Mader, C., and M. Gittings (2002), Modelling of the 1958 Lituya Bay mega-tsunami. ii, *Sci. Tsunami Hazards*, *20*(5), 241–250.

Masson, D., A. Watts, M. Gee, R. Urgeles, N. Mitchell, T. Le Bas, and M. Canals (2002), Slope failures on the flanks of the western Canary Islands, *Earth Sci. Rev.*, *57*, 1–35.

Masson, D. G., C. B. Harbitz, R. B. Wynn, G. Pedersen, and F. Løvholt (2006), Submarine landslides -processes, triggers and hazard prediction, *Philos. Trans. R. Soc.*, *A364*, 2009–2039.

Mei, C. C. (1989), *The Applied Dynamics of Ocean Surface Waves*, World Sci., Hackensack, N. J.

Mesinger, F., and A. Arakawa (1976), Numerical methods used in atmospheric models, *GARP Publ. Ser. WMO*, *17*, 1–64.

Miles, J. W. (1980), Solitary waves, *Ann. Rev. Fluid Mech.*, *12*, 11–43.

Miller, D. (1960), Giant waves in Lituya Bay, Alaska, *Geol. Surv. Prof. Pap.*, *354-C*.

Moore, J. G., D. A. Clague, R. T. Holcomp, P. W. Lipman, W. R. Normark, and M. E. Torresan (1989), Prodigious submarine landslides on the Hawaiian Ridge, *J. Geophys. Res.*, *94*, 17,465–17,484.

Nadim, F., and T. Glade (2006), On tsunami risk assessment for the west coast of Thailand, in *ECI Symposium Series*, vol. *7*, edited by F. Nadim, R. Pöttler, H. Einstein, H. Klapperich, and S. Kramer.

Nwogu, O. (1993), Alternative form of Boussinesq equations for near-shore wave propagation, *J. Waterw. Port Coastal Ocean Eng.*, *119*(6), 618–638.

Pararas-Carayannis, G. (2002), Evaluation of the threat of mega tsunami generation from postulated massive slope failures of island stratovolcanoes on La Palma, Canary Islands, and on the island of Hawaii, *Sci. Tsunami Hazards*, *20*(5), 251–277.

Pedersen, G. (1991), Finite difference representations of nonlinear waves, *Int. J. Numer. Methods Fluids*, *13*, 671–690.

Pedersen, G., and F. Løvholt (2008), Documentation of a global Boussinesq solver, in *Preprint Series in Applied Mathematics 1*, Dep. of Math., Univ. of Oslo, Oslo, Norway. (Available at http://www.math.uio.no/eprint/appl_math/2008/01-08.html)

Pedersen, G., and O. B. Rygg (1987), Numerical solution of the three dimensional Boussinesq equations for dispersive surface waves, in *Preprint Series in Applied Mathematics*, Dep. of Math., Univ. of Oslo, Oslo, Norway.

Peregrine, D. (1966), Calculation of the development of an andular bore, *J. Fluid Mech.*, *22*(2), 321–330.

Peregrine, D. H. (1967), Long waves on a beach, *J. Fluid Mech.*, *77*, 417–431.

Perignon, Y. (2006), Tsunami hazard modelling, Master thesis, Univ. of Rhode Island and Ecole Centrale de Nantes.

Perla, R., T. Cheng, and D. McClung (1980), A two-parameter model of snow-avalance motion, *J. Glaciol.*, *26*(94), 197–207.

Rygg, O. B. (1988), Nonlinear refraction-diffraction of surface waves in intermediate and shallow water, *Coastal Eng.*, *12*, 191–211.

Shi, F., R. A. Dalrymple, J. T. Kirby, Q. Chen, and A. Kennedy (2001), A fully nonlinear boussinesq model in generalized curvilinear coordinates, *Coastal Eng.*, *42*, 337–358.

Shuto, N. (1985), The Nihonkai-Chubu earthquake tsunami on the north Akita Coast, *Coastal Eng. Jpn.*, *28*, 255–264.

Tappin, D., P. Watts, and S. T. Grilli (2008), The Papua New Guinea tsunami of 17 July 1998: Anatomy of a chatastrophic event, *Nat. Hazards Earth Syst. Sci.*, *8*, 243–266.

Tinti, S., A. Armigliato, A. Manucci, G. Pagnoni, and F. Zaniboni (2005), Landslides and tsunamis of December, 2002 at Stromboli, Italia: Numerical simulations, *Boll. Geofis. Teor. Appl.*, *46*(2).

Titov, V. V., and C. E. Synolakis (1997), Extreme inundation flows during the Hokkaido-Nansei-Oki tsunami, *Geophys. Res. Lett.*, *24*(11), 1315–1318.

Titov, V. V., and C. E. Synolakis (1998), Numerical modeling of tidal wave runup, *J. Waterway Port Coastal Ocean Eng.*, *124*(4), 157–171.

Walder, J., P. Watts, O. Sorensen, and K. Janssen (2003), Tsunamis generated by subaerial mass flows, *J. Geophys. Res.*, *108*(B5), 2236, doi:10.1029/2001JB000707.

Ward, S. N., and S. Day (2001), Cumbre Vieja volcano – Potential collapse and tsunami at La Palma, Canary Islands, *Geophys. Res. Lett.*, *28*(17), 3397–3400.

Wei, G., J. T. Kirby, S. T. Grilli, and R. Subramanya (1995), A fully nonlinear boussinesq model for surface waves. Part 1. Highly nonlinear unsteady waves, *J. Fluid Mech.*, *294*, 71–92.

Wynn, R., and D. Masson (2003), Canary Islands landslides and tsunami generation: Can we use turbidite deposits to interpret landslide processes, in *Submarine Mass Movements and Their Consequences*, edited by J. Locat and J. Mienert, pp. 325–332, Kluwer Acad., Dordrecht, Netherlands.

G. Gisler, Physics Department, University of Oslo, 0316 Oslo, Norway.

F. Løvholt, Computational Geomechanics Division, Norwegian Geotechnical Institute, P.O. Box 3930, Ullevål Stadion, 0806 Oslo, Norway. (flo@ngi.no)

G. Pedersen, Department of Mathematics, University of Oslo, 0316 Oslo, Norway.